

# High-Resolution Polarimetric Radar Observations of Snow-Generating Cells

MATTHEW R. KUMJIAN\*

*Advanced Study Program, National Center for Atmospheric Research,<sup>+</sup> Boulder, Colorado*

STEVEN A. RUTLEDGE

*Department of Atmospheric Science, Colorado State University, Fort Collins, Colorado*

ROY M. RASMUSSEN

*Research Applications Laboratory, National Center for Atmospheric Research, Boulder, Colorado*

PATRICK C. KENNEDY

*Department of Atmospheric Science, Colorado State University, Fort Collins, Colorado*

MIKE DIXON

*Research Applications Laboratory, National Center for Atmospheric Research, Boulder, Colorado*

(Manuscript received 9 October 2013, in final form 30 January 2014)

## ABSTRACT

High-resolution X-band polarimetric radar data were collected in 19 snowstorms over northern Colorado in early 2013 as part of the Front Range Orographic Storms (FROST) project. In each case, small, vertically erect convective turrets were observed near the echo top. These “generating cells” are similar to those reported in the literature and are characterized by  $\sim 1$ -km horizontal and vertical dimensions, vertical velocities of  $1\text{--}2\text{ m s}^{-1}$ , and lifetimes of at least 10 min. In some cases, these generating cells are enshrouded by enhanced differential reflectivity  $Z_{DR}$ , indicating a “shroud” of pristine crystals enveloping the larger, more isotropic particles. The anticorrelation of radar reflectivity factor at horizontal polarization  $Z_H$  and  $Z_{DR}$  suggests ongoing aggregation or riming of particles in the core of generating cells. For cases in which radiosonde data were collected, potential instability was found within the layer in which generating cells were observed. The persistence of these layers suggests that radiative effects are important, perhaps by some combination of cloud-top cooling and release of latent enthalpy through depositional and riming growth of particles within the cloud. The implications for the ubiquity of generating cells and their role as a mechanism for ice crystal initiation and growth are discussed.

## 1. Introduction

During the 2013 snow season in north-central Colorado (January–May), scientists at the National Center for

Atmospheric Research (NCAR) and Colorado State University (CSU) ran a pilot field experiment to study the finescale structure of winter storms. Called the Front Range Orographic Storms (FROST) project, the study involved intensive radar measurements that were taken during winter precipitation events. FROST leveraged the ongoing Solid Precipitation Intercomparison Experiment (SPICE; <http://www.wmo.int/pages/prog/www/IMOP/intercomparisons.html>), which aims to quantify uncertainty associated with snow gauge measurements of winter precipitation, with the eventual goal of improving quantitative precipitation estimates. As part of SPICE, NCAR has deployed a suite of automated snow gauges at its Marshall Field Site (MFS) in north-central Colorado ([Rasmussen](#)

---

\* Current affiliation: Department of Meteorology, The Pennsylvania State University, University Park, Pennsylvania.

<sup>+</sup> The National Center for Atmospheric Research is sponsored by the National Science Foundation.

---

*Corresponding author address:* Dr. Matthew R. Kumjian, Dept. of Meteorology, The Pennsylvania State University, 513 Walker, University Park, PA 16802.  
E-mail: [kumjian@psu.edu](mailto:kumjian@psu.edu)

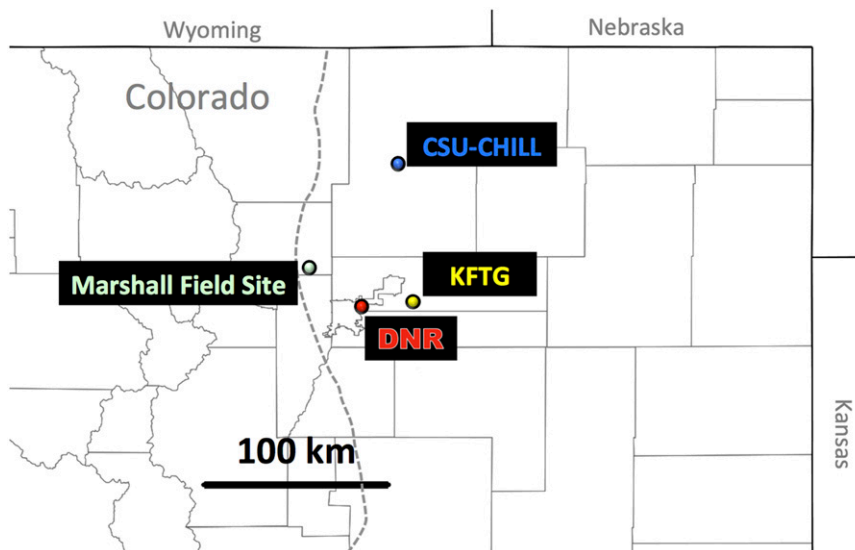


FIG. 1. Map of the FROST domain in northeastern Colorado, with facilities noted: the CSU-CHILL radar, MFS, the WSR-88D radar at KFTG, and the sounding site at DNR. The gray dashed line shows the edge of the Front Range of the Rocky Mountains.

et al. 2012; Fig. 1). MFS, nestled against the Front Range of the Rocky Mountains, also served as the central facility for operations during FROST.

The main goals of FROST-2013 were to investigate the finescale structure of winter storms along the Colorado Front Range, to document and quantify the microphysical processes occurring in such storms, and to relate remotely sensed quantities to the surface precipitation type and intensity, capitalizing on the rich surface datasets available from SPICE. FROST employed two X-band polarimetric radars with specialized scanning strategies. The two X-band radars used were CSU's University of Chicago–Illinois State Water Survey radar (CSU-CHILL; Bringi et al. 2011) and NCAR's mobile X-band polarimetric radar (NCAR-XPOL; see the appendix for details). In addition to these research radars, routine surveillance scan data from the National Weather Service Weather Surveillance Radar-1988 Doppler (WSR-88D) near Denver, Colorado (KFTG), were available. All radars used for FROST are dual polarization, operating in the mode of simultaneous transmission and reception of horizontally and vertically polarized waves. This mode of operation allows for the measurements of radar reflectivity factor at horizontal polarization  $Z_H$ ; differential reflectivity  $Z_{DR}$ ; differential propagation phase shift  $\Phi_{DP}$ , from which the specific differential phase  $K_{DP}$  is calculated by following the method of Wang and Chandrasekar (2009); and the copolar correlation coefficient  $\rho_{hv}$ . More information on the polarimetric radar variables can be found in the textbooks of Doviak and Zrnić (1993) and Bringi and Chandrasekar (2001), as well

as the studies by Zrnić and Ryzhkov (1999), Straka et al. (2000), Ryzhkov et al. (2005), and Kumjian (2013a–c). In addition to the radar data, special radiosondes were launched from MFS during storm events. These supplemented the regular National Weather Service soundings taken two times per day from near Denver (DNR). Figure 1 shows the relative locations of the X-band radars (NCAR-XPOL is at MFS), KFTG, and DNR.

CSU-CHILL was recently outfitted to have dual-wavelength capabilities by adding an X-band transmitter to the preexisting S-band transmitter (e.g., Junyent et al. 2013; F. Junyent et al. 2014, manuscript submitted to *Bull. Amer. Meteor. Soc.*). For the purposes of this study, we selected the use of “X-band only” mode, which features a very narrow beamwidth ( $0.3^\circ$ ), large antenna gain (54.3 dB; the CHILL antenna is 8.5 m in diameter), and extreme cross-polar isolation ( $-45$  dB). These characteristics allow for high quality, very finescale observations of winter precipitation. The X-band mode was chosen because 1) attenuation and non-Rayleigh scattering effects that often plague X-band radar observations in warm-season precipitation events are not as prevalent in winter snowstorms and 2) the shorter wavelength results in larger  $K_{DP}$ , allowing for better detection of dendritic growth zones (e.g., Kennedy and Rutledge 2011; Andrić et al. 2013; Schneebeli et al. 2013; Bechini et al. 2013). The dual-PRF strategy employed during FROST allowed for a good maximum range ( $>90$  km) and a Nyquist interval of  $\pm 23.9 \text{ m s}^{-1}$  (F. Junyent et al. 2014, manuscript submitted to *Bull. Amer. Meteor. Soc.*).

TABLE 1. Data-collection times (UTC) of the CSU-CHILL radar, NCAR-XPOL radar at MFS, and the special radiosondes launched from MFS for events from the FROST-2013 experiment.

CSU-CHILL	NCAR-XPOL	MFS radiosondes
1536–2314 11 Jan	—	—
1916 28 Jan–1624 29 Jan	—	—
2100–2137 31 Jan	—	—
2224–2355 6 Feb	0009–2359 6 Feb	—
2150 9 Feb–0906 10 Feb	0000 9 Feb–2359 10 Feb	—
2150–2206 11 Feb	0000–2359 11 Feb	—
1712 14 Feb–0036 15 Feb	1815 14 Feb–1859 15 Feb	—
1616 20 Feb–1914 21 Feb	1658 20 Feb–0226 21 Feb; 1618–2359 21 Feb	2022 and 2250 20 Feb; 0017 21 Feb
0006 24 Feb–0307 25 Feb	0000 24 Feb–2359 25 Feb	—
1653–2115 4 Mar	1922–2359 4 Mar	—
1757–1825 8 Mar	—	—
0248–2259 9 Mar	0300–2359 9 Mar	0415, 0605, 1057, 1242, and 1319 9 Mar
2013 22 Mar–1739 23 Mar	1713 22 Mar–2359 23 Mar	—
2139 8 Apr–2234 9 Apr	—	0148, 0323, and 0820 9 Apr
1805–2007 12 Apr	—	—
1530 15 Apr–1300 16 Apr	—	—
1514 17 Apr–0233 18 Apr	—	—
1556 22 Apr–0635 23 Apr	—	—
0000–2246 1 May	0000–2359 1 May	—

The FROST-2013 experiment collected data during a total of 19 cases, although not all instrumentation was available for each case (see Table 1 for details). For most of these cases, the research radars operated using specified scanning strategies. The scanning strategy for the NCAR-XPOL radar involved 10 PPI scans at constant elevation angles, 10 RHI scans at constant azimuth angles, and 3 min of vertically pointing or “birdbath” scans. CSU-CHILL volume scans comprised six PPI sweeps followed by four RHIs (including one over MFS). Table 2 has the details of each radar’s scanning strategy. Note that in some cases the scanning strategies were changed at the discretion of the radar operator and/or the principal investigators (PIs) in an effort to capture targets of opportunity, including continuous RHIs to capture more rapid updates on the evolution of features of interest.

One such feature of interest that was observed in every case during FROST is a collection of small-scale, vertically erect turrets located near echo top (Fig. 2). These turrets are reminiscent of so-called generating cells that produce high concentrations of ice crystals near cloud top. Such generating cells near cloud top have been documented in the literature for over 50 years, as

discussed in detail in the next section. However, the unique high-resolution polarimetric radar measurements coupled with in situ thermodynamic data from the radiosondes provide a detailed look at the structure and evolution of these generating cells—and in a larger number of cases than previously documented. In addition, the use of polarimetric radar data in this study reveals added information regarding the microphysical composition of generating cells, including what we term a “shroud echo” surrounding some of the generating cells.

The next section reviews previous studies that have documented generating cells. Section 3 presents observational data from FROST of generating cells and shroud echoes and provides microphysical explanations for their appearance. The practical implications of generating cells and shroud echoes are discussed in section 4, which is followed by a summary of our main conclusions in section 5.

## 2. Background

For over half of a century, observations of so-called generating cells of cloud and precipitation particles and their associated fall streaks have been presented in the

TABLE 2. Standard scanning strategies for the research radars during FROST. Scanning strategies were subject to change at the discretion of the PIs and radar operators.

Radar	PPIs (°)	RHIs (°)	Birdbath scans
NCAR-XPOL	1.1, 2.1, 3.1, 4.1, 5.1, 6.0, 7.0, 8.1, 9.0, and 9.9	95.0, 105.0, 115.0, 125.0, 135.0, 145.0, 155.0, 165.0, 175.0, and 180.0	3 min
CSU-CHILL	0.4, 0.9, 1.7, 2.8, 3.9, and 5.0	235.8, 220.7, 214.4, and 181.8	None

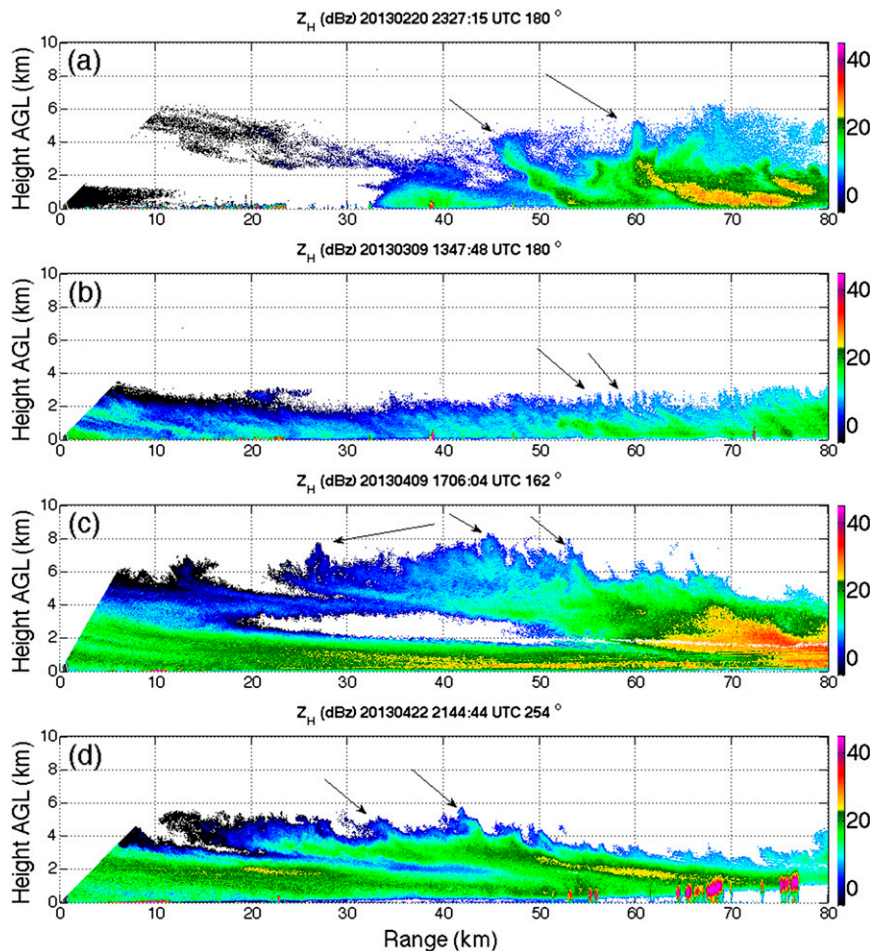


FIG. 2. Examples of generating cells observed by CSU-CHILL RHIs of  $Z_H$  on four different days: (a) 2327:15 UTC 20 Feb 2013 along azimuth  $180^\circ$ , (b) 1347:48 UTC 9 Mar 2013 along azimuth  $180^\circ$ , (c) 1706:04 UTC 9 Apr 2013 along azimuth  $162^\circ$ , and (d) 2144:44 UTC 22 Apr 2013 along azimuth  $254^\circ$ . Arrows in each panel indicate the locations of some of the generating cells.

literature (e.g., Marshall 1953; Gunn et al. 1954; Langleben 1956; Miles 1956; Ludlam 1956; Douglas et al. 1957; Wexler and Atlas 1959, and many others). These cells seem to play an important role in the production of precipitation that eventually reaches the surface (e.g., Douglas et al. 1957; Hobbs and Locatelli 1978; Matejka et al. 1980; Herzegh and Hobbs 1981; Houze et al. 1981; Rutledge and Hobbs 1983). The generating cells are small-scale convective towers that are often located at or near cloud top. Most previous studies are consistent in reporting horizontal dimensions on the order of 1–2 km, with vertical extents of slightly less than that (see Table 3). Updraft speeds have been estimated or inferred from measurements in various ways but have been consistently reported at about  $1 \text{ m s}^{-1}$ . Cronic et al. (2007) report a maximum updraft speed in a winter snowband of  $\sim 6 \text{ m s}^{-1}$ ; however, they also show that only 9% of their profiler observations revealed updrafts exceeding  $2 \text{ m s}^{-1}$ .

In contrast to the width, depth, and intensity of generating cells, there appears to be no preferred height or temperature level at which they form (e.g., Douglas et al. 1957). For example, Crosier et al. (2013) found them at temperatures that were colder than  $-40^\circ\text{C}$ , whereas Henrion et al. (1978) found them near  $-12^\circ\text{C}$ . Evans et al. (2005) even found generating cells located at two different levels during the same event (at about  $-21^\circ\text{C}$  and at temperatures below  $-40^\circ\text{C}$ ). In a similar way, the literature is inconsistent regarding the characteristic spacing between generating cells, with a range of values between about 5 (Wexler and Atlas 1959; Sassen et al. 1990) and 32 (Marshall 1953) km. One study (Syrett et al. 1995) even found the spacing to change from 1.8 to 12 km after the passage of an upper-level trough. The apparent lack of preferred spacing or location implies that the physical processes producing generating cells are not dependent on temperature or microphysics

TABLE 3. Selected physical characteristics of generating cells as reported in the literature.

Source	Horizontal extent	Vertical extent	Updraft speed
Langleben (1956)	~1.6 km	~1.6 km	
Douglas et al. (1957)		<1.6 km	1–3 m s <sup>-1</sup>
Wexler and Atlas (1959)		<1.6 km	<1 m s <sup>-1</sup>
Browning and Harrold (1969)	A few kilometers		0.8 m s <sup>-1</sup>
Heymsfield and Knollenberg (1972)	1–2 km	1 km	
Carbone and Bohne (1975)			~2 m s <sup>-1</sup>
Houze et al. (1976)	~1 km	~1 km	
Henrion et al. (1978)	1–2 km	0.5–0.7 km	
Herzogh and Hobbs (1981)	3–6 km	1–2 km	1.1 m s <sup>-1</sup>
Houze et al. (1981)	~1.5 km	~1.5 km	
Sassen et al. (1990)	1–2 km		
Wolde and Vali (2001)	Hundreds of meters to 1 km		~2 m s <sup>-1</sup>
Cronce et al. (2007)			Up to 6 m s <sup>-1</sup>
Crosier et al. (2013)			1–2 m s <sup>-1</sup>
Stark et al. (2013)			<1 m s <sup>-1</sup>

and are unlikely to be caused by wavelike or other periodically varying kinematic features.

Most of the studies are in agreement that lifting of potentially unstable air at cloud top is the source of the convective instability that drives the generating cells. A notable exception is Ludlam (1956), who suggests that release of latent enthalpy by depositional growth of ice crystals in the fall streaks leads to buoyant air that rises up the fall streak and forms the “shred cloud” associated with the fall streak. In other words, Ludlam (1956) argues that the fall streaks cause the generating cells. Syrett et al. (1995) present interesting cloud-radar observations of a thinned cirrus layer above the generating cells. They posit that enhanced radiational cooling afforded by thinning of the overlying cirrus cloud may have allowed the formation of the generating cells.

The majority of the generating-cell observations come from remote sensing platforms, such as cloud and precipitation radars, lidars, and profilers. There is general agreement that the higher reflectivity [or signal-to-noise ratio (SNR)] core of the generating cell is associated with updraft, while compensating downdrafts on the periphery of the cells are found in regions of low reflectivity or SNR (e.g., Carbone and Bohne 1975; Cronce et al. 2007). This observation implies that precipitation particles being generated in the generating cells are falling back through the updraft once they have grown to sufficiently large sizes (Carbone and Bohne 1975).

Indeed, aircraft penetrations have revealed enhanced ice crystal number concentration within generating cells (e.g., Henrion et al. 1978; Houze et al. 1981; Wolde and Vali 2001; Evans et al. 2005; Ikeda et al. 2007; Crosier et al. 2013). In many of these cases, liquid water droplets were detected and/or icing of the aircraft or its probes occurred (Wexler and Atlas 1959; Henrion et al. 1978; Houze et al. 1981; Wolde and Vali 2001; Evans et al.

2005; Ikeda et al. 2007; Rosenow et al. 2014), suggesting that updrafts were sufficiently strong to sustain supercooled liquid water, even in the presence of significant ice water contents.

With this historical context in mind, we present our FROST observations of generating cells and shroud echoes in the following section. We address the following main scientific questions in this study: How prevalent are generating cells in winter storms over northern Colorado? What are plausible mechanisms for their formation? What are the physical and microphysical characteristics of these generating cells? Could such characteristics provide information about the presence of supercooled liquid water in winter clouds?

### 3. FROST observations

#### a. Synoptic overview

All of the major events from the FROST dataset exhibited very similar synoptic environments. Such a setup is reminiscent of previous studies of winter events in Colorado (e.g., Rasmussen et al. 1995, among others) and is conducive to the production of shallow (~2 km thick or less) upslope precipitating clouds. As an example, the salient synoptic features from the 9 April 2013 event are shown in Fig. 3, valid at 1200 UTC. Subzero temperatures associated with an Arctic air mass were in place over much of Colorado after the passage of the cold front. The cold front was associated with an upper-level trough approaching from the southwest, which at 1200 UTC was centered approximately on the Four Corners region of the southwestern United States. The strong northeasterly surface flow behind the front allowed for the shallow upslope cloud to form. The large-scale ascent associated with the downstream portion of the upper-level trough is suspected to play an important

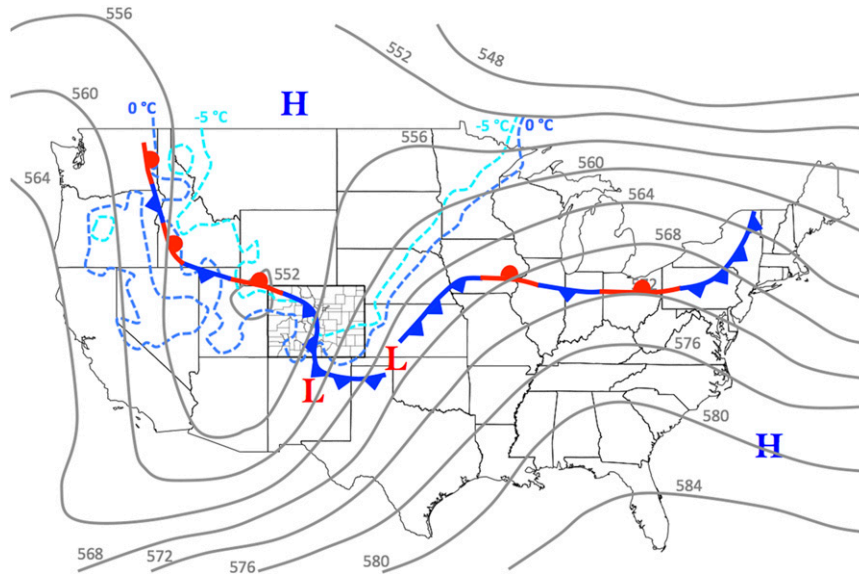


FIG. 3. Synoptic overview of the 9 Apr 2013 case, showing salient features valid at 1200 UTC. The gray contours show the objectively analyzed 500-hPa heights in dekameters. Also shown are subjectively analyzed surface fronts, surface pressure centers, and the surface  $0^{\circ}$  and  $-5^{\circ}\text{C}$  isotherms. Subjective analysis of the surface features is based on analyses by the Hydrometeorological Prediction Center and the Storm Prediction Center.

role in triggering the generating cells, which are described next.

#### b. Generating cells

Despite using predetermined scanning strategies during most of the data collection efforts as well as overnight unattended operations by both X-band radars, generating cells were found in every case in FROST, evident in the limited number of RHI scanning directions selected. This means that they are likely very common in winter precipitation, if not ubiquitous. In agreement with Douglas et al. (1957) and the literature review presented in the previous section, there was no preferred height or temperature level at which the generating cells appeared; they were observed at heights ranging from 3.0 to 8.0 km (cf. Fig. 2), which corresponds to temperatures ranging from approximately  $-12^{\circ}\text{C}$  to colder than  $-40^{\circ}\text{C}$ . Figure 2 also reveals that their frequency and spacing varied considerably as well.

The widths of individual turrets generally was less variable, with most on the order of  $\sim 1$  km or less in girth, as visually estimated from the  $Z_H$  field in RHI scans. In some cases, the individual turrets remained distinct in the  $Z_H$  field for up to  $\sim 1$  km in height (e.g., Fig. 4). Note that at least some of the variability in these characteristics can be attributed to differences in how the radar cross sections intersected the generating cells in the different cases. In addition, the radar may not give a complete picture, as there may be portions of generating cells

without particles large enough to be detectable by radar. Such regions (e.g., supercooled cloud droplets) could still be microphysically important.

The  $Z_{DR}$  field in Fig. 4 also shows that microphysical variability is possible even at the same height or temperature level within a given case, strongly suggesting that differences in supersaturation, riming, aggregation, and so on may occur within different generating cells. In a typical case, fall streaks were observed descending from the more mature generating cells as snow fell into the underlying layer of sheared flow.

Figures 5a and 5c are of a PPI scan taken at a higher elevation angle ( $4.99^{\circ}$ ) such that the beam transects the generating cells. An RHI overlaid with the beam propagation path through some of the generating cells at that elevation angle is provided in Figs. 5b and 5d. It demonstrates the lack of preferred spacing or orientation of the generating cells in plan view, as well as their convective appearance. As mentioned in the previous section, the lack of any well-defined periodic structure or orientation to their spacing strongly suggests that the generating cells are convective in nature and are not forced by any wavelike kinematic features. The PPI scan also reveals that the generating cells are roughly isotropic in the horizontal plane. Thus, the characteristic scales inferred from the RHI scans (which provide a better view of their horizontal dimension) should not depend on viewing angle and should be valid for both horizontal dimensions of the generating cells.

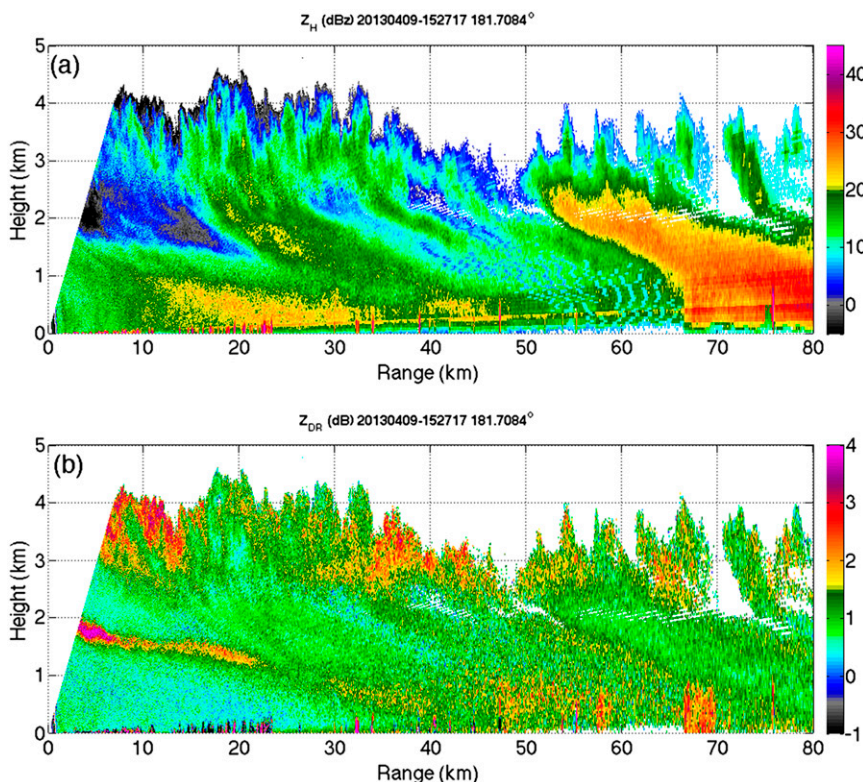


FIG. 4. An example of generating cells observed by CSU-CHILL at 1527 UTC 9 Apr 2013. The vertical cross section is taken along azimuth 181.7°. Shown are (a)  $Z_H$  and (b)  $Z_{DR}$ .

Also note the two distinct precipitation regimes evident in Fig. 5. The first is a shallow layer (<2 km) near the ground formed by upslope flow, topped by a thin band of enhanced  $Z_{DR}$  values approaching 3 dB. Beneath this enhanced  $Z_{DR}$ ,  $Z_H$  increases toward the ground, coincident with a decrease in  $Z_{DR}$ . These signatures indicate pristine anisotropic ice crystals near the top of this layer, followed by aggregation of the crystals as they descend. From the 1200 UTC operational sounding launched from DNR before the radar scan, it is observed that the temperature at this low-level (1.5–2.0 km AGL) enhanced  $Z_{DR}$  band is about  $-15^{\circ}\text{C}$ . Thus, dendritic or platelike crystals are likely, depending on the saturation levels supported by the weak updrafts. Because of the rapid aggregation suggested by the polarimetric radar observations, dendrites seem to be the most likely habit.

Overlying this shallow layer are vertically erect generating cells between about 3 and 4 km AGL. Some of the generating cells are characterized by very large  $Z_{DR}$  values of more than 4 dB. The sounding-inferred temperature in this layer is from approximately  $-12^{\circ}$  to  $-18^{\circ}\text{C}$ , and therefore dendritic or platelike crystals again are likely being generated within the generating cells. The double  $-15^{\circ}\text{C}$  layers (and thus double layers

of enhanced  $Z_{DR}$ ) reveal the complex thermodynamic and microphysical structure of some of these winter cases. The highest  $Z_{DR}$  values correspond to lower  $Z_H$  values, possibly indicating that smaller platelike crystals are growing in weaker and/or younger generating cells characterized by smaller supersaturations. Such plates are inefficient at aggregation, allowing the generating cells to maintain the high  $Z_{DR}$  and low  $Z_H$  values. In contrast, the higher- $Z_H$ , lower- $Z_{DR}$  cells could be indicative of dendrites growing in larger supersaturations produced by stronger or more mature generating cells. Such dendrites more readily aggregate, producing larger  $Z_H$  and lower  $Z_{DR}$ . In addition, the stronger updrafts are also those most likely to support supercooled liquid water and the potential for particle growth by riming.

Indeed, the microphysical structure of the generating cells is governed by the temperature in which they form and the supersaturations they can maintain. In selected cases, the special soundings launched from MFS using CSU's Vaisala, Inc., sounding system allowed for an investigation of the environmental characteristics in which generating cells occurred. To investigate this microphysical dependence on temperature, RHI scans over MFS (at an azimuth of 220.7°) were selected if they occurred within 10 min prior to or 20 min after the

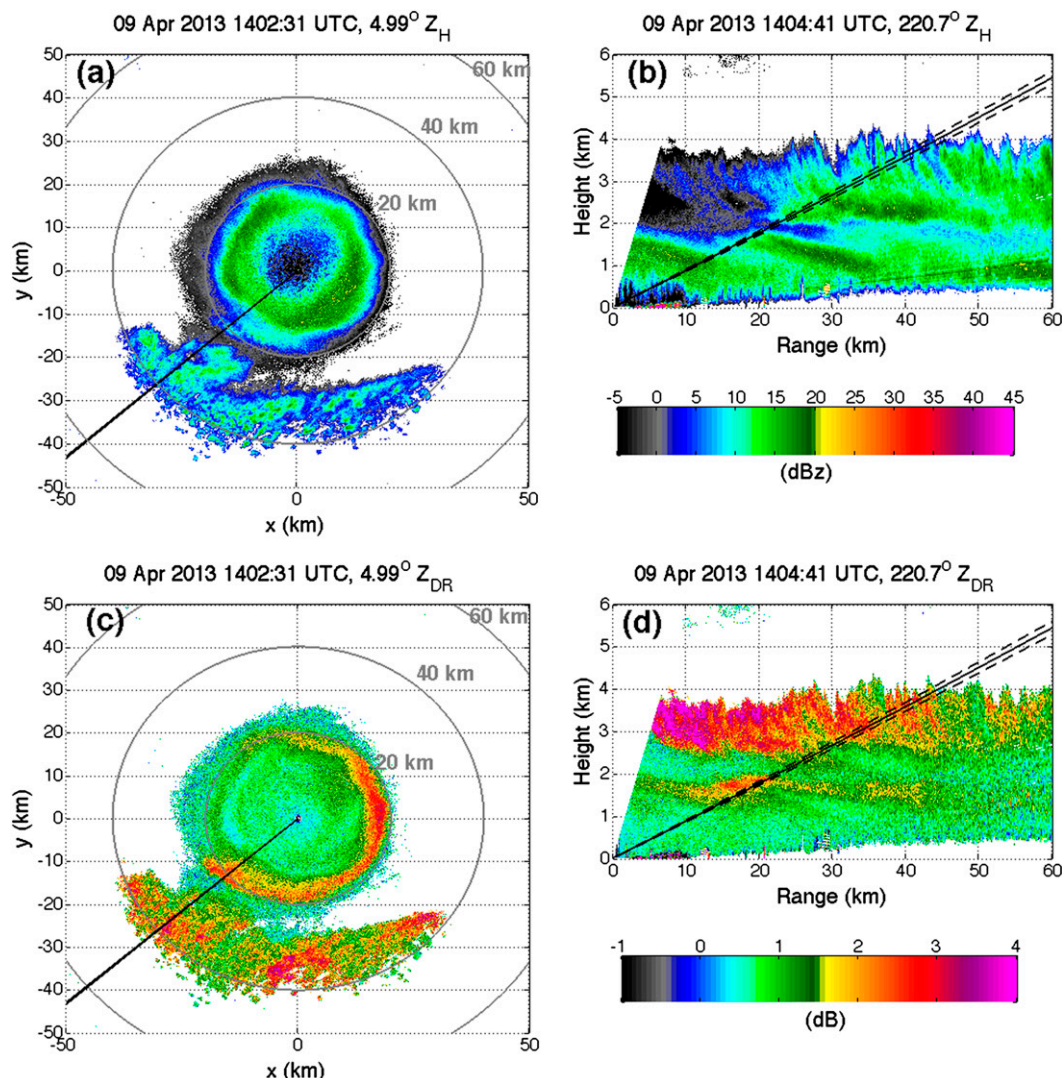


FIG. 5. The  $4.99^\circ$ -elevation-angle PPI scans showing (a)  $Z_H$  and (c)  $Z_{DR}$  at 1402:31 UTC 9 Apr 2013, taken by CSU-CHILL. Range rings are provided every 20 km. The black line indicates the azimuth along which the RHIs in the right column were taken. RHIs show fields of (b)  $Z_H$  and (d)  $Z_{DR}$  along azimuth  $220.7^\circ$  taken by CSU-CHILL at 1404:41 UTC 9 Apr 2013. The solid line indicates the approximate beam path at  $4.99^\circ$  elevation angle, with the dashed lines indicating the top and bottom of the  $0.3^\circ$  beam.

sounding launch time. These selection criteria were chosen in an attempt to maximize the representativeness of the sounding-observed temperatures; there is no guarantee, however, that the sounding is entirely representative over the large area sampled by the RHI scans. The data from altitudes of greater than 1 km AGL and between 10- and 80-km range were chosen to minimize contamination from ground clutter, beam blockage, and the terrain at far ranges. In addition, a normalized coherent power threshold of 0.25 was chosen to ensure radar volumes of sufficiently good quality. The resulting radar volumes were binned according to the MFS-sounding-observed temperature in  $0.2^\circ\text{C}$  bins, for

each of which the median  $Z_{DR}$  and 0.05 and 0.95 quantiles of  $Z_{DR}$  were computed. Also, the  $Z_{DR}$  data were put into 0.2-dB bins, and a normalized frequency distribution was constructed (normalized by the largest frequency within a  $0.2^\circ\text{C}$  bin such that the maximum frequency in each  $0.2^\circ\text{C}$  bin is 1.0). The results for the 9 March 2013 case are shown in Fig. 6.

It is clear that a much wider distribution is found centered on a temperature of approximately  $-15^\circ\text{C}$ , corresponding to platelike or dendritic growth. The distribution around this temperature is strongly skewed toward larger  $Z_{DR}$  values. The median and 5%–95% bounds are also slightly shifted to larger  $Z_{DR}$  values at

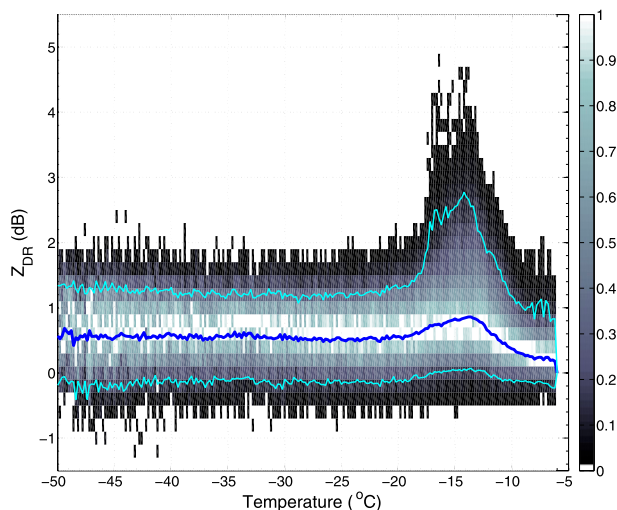


FIG. 6. Normalized frequency distribution of CSU-CHILL-observed  $Z_{DR}$  values vs the temperature for those radar volumes as observed by the MFS soundings launched at 1057 and 1319 UTC 9 Mar 2013. Only radar data collected along the azimuth over MFS from within 10 min prior to and 20 min after the sounding launch time are used in the analysis. Data are binned into  $0.2^{\circ}\text{C} \times 0.2$  dB bins. Overlaid are the median  $Z_{DR}$  (dark blue line) and 5th and 95th percentiles of  $Z_{DR}$  (thin cyan lines) for each  $0.2^{\circ}\text{C}$  bin.

these temperatures. The radar volumes recording  $Z_{DR}$  values in excess of 4–5 dB require the presence of high-density crystals such as plates, whereas dendrites tend to produce more modest (but still enhanced)  $Z_{DR}$  values (e.g., Hogan et al. 2002; Kennedy and Rutledge 2011; Andrić et al. 2013; Schneebeli et al. 2013). At colder temperatures, the distribution is remarkably flat, centered on much lower  $Z_{DR}$  values—a situation that is indicative of more isometric crystals. At temperatures that are warmer than approximately  $-15^{\circ}\text{C}$ , the median  $Z_{DR}$  and peak of the  $Z_{DR}$  distribution drop to lower values, likely indicative of aggregation of the dendritic crystals located above.

This analysis was repeated for each sounding time. The expanded distribution at  $-15^{\circ}\text{C}$  was not as pronounced or sometimes not even present in each case; rather, the distribution was similar to that at colder temperatures (not shown). This may be because crystals were initiated and grown at colder temperatures and simply descended into warmer temperatures without growth (i.e., conditions were not favorable for ice crystal growth at these levels at these times).

Selected data from radiosondes launched from MFS during snowstorms are shown in Fig. 7. In each instance, small dewpoint depressions characterize the majority of the troposphere, suggesting the storms were characterized by deep clouds at the times of the soundings. In at least two of the cases (21 February and 9 April), an indication of shallow upslope flow is present, suggested by

the low-level cold layer with northeasterly flow overtopped by a strong inversion. As discussed above, many of the previous studies have posited lifting of convectively unstable parcels as the mechanism by which generating cells form. To diagnose regions of potential instability, the vertical profile of equivalent potential temperature  $\theta_e$  and its vertical gradient are computed (Fig. 8) from the sounding measurements by following the method of Lamb and Verlinde (2011). (Note that use of the equivalent potential temperature with respect to ice, or  $\theta_{ei}$ , may also be used for snowstorms. We chose to use the more conservative  $\theta_e$ , which provides a more stringent criterion for the detection of regions of potential instability.) Potential instability exists where  $\theta_e$  decreases with increasing height (i.e., where  $\partial\theta_e/\partial z < 0$ ). In the 20–21 February 2013 case (Figs. 8a,b), there are several regions of potential instability in the layer between approximately 3.75 and 7.0 km, with the largest magnitude of just below  $2\text{ K km}^{-1}$  being located at  $\sim 3.75$  km.

Vertical cross sections from CSU-CHILL (Fig. 9) reveal generating cells in this layer, which is consistent with the sounding-observed regions of potential instability. Note that the vertical extent of generating cells at farther ranges ( $>70$  km) is likely underestimated, as the top portions of the cells fall below the minimum detectable reflectivity at those ranges. Enhancements of  $Z_{DR}$  and  $K_{DP}$  are evident in the top portions of the generating cells (Figs. 9b,c), roughly centered at  $\sim 3$ – $4$ -km height. Maximum  $K_{DP}$  values exceeded  $1.5^{\circ}\text{ km}^{-1}$ , indicating sufficiently large concentrations of anisotropic crystals. The 0017 UTC sounding at MFS (cf. Fig. 7a) indicated a temperature at 3 km (4 km) AGL of  $-18.3^{\circ}\text{C}$  ( $-26.3^{\circ}\text{C}$ ). Thus, the enhanced polarimetric signatures at these temperatures are consistent with growth of platelike or dendritic snow crystals (e.g., Kennedy and Rutledge 2011; Andrić et al. 2013; Bechini et al. 2013). Indeed, near this time the sounding crew at MFS observed small ( $<2$  mm) dendrites at the surface, mixed with small, irregular crystals.

A time–height display of vertically pointing NCAR-XPOL  $Z_H$  and Doppler velocity measurements over a 3-min period beginning at 2355 UTC (Fig. 10) reveals positive Doppler velocities (up to  $1\text{ m s}^{-1}$ ) associated with weak  $Z_H$  ( $<5$  dBZ) above  $\sim 3.75$  km, consistent with the depth (diagnosed from the sounding) containing potential instability. The mean Doppler velocity over the 3-min period was positive above  $\sim 4.4$  km (Fig. 10c). Note that the measured vertical Doppler velocity is a combination of particle fall speed and air motion; thus, the actual vertical air motion is somewhat higher than measured (i.e.,  $>1\text{ m s}^{-1}$ ). This vertical velocity estimate is consistent with the values reported in the literature reviewed above.

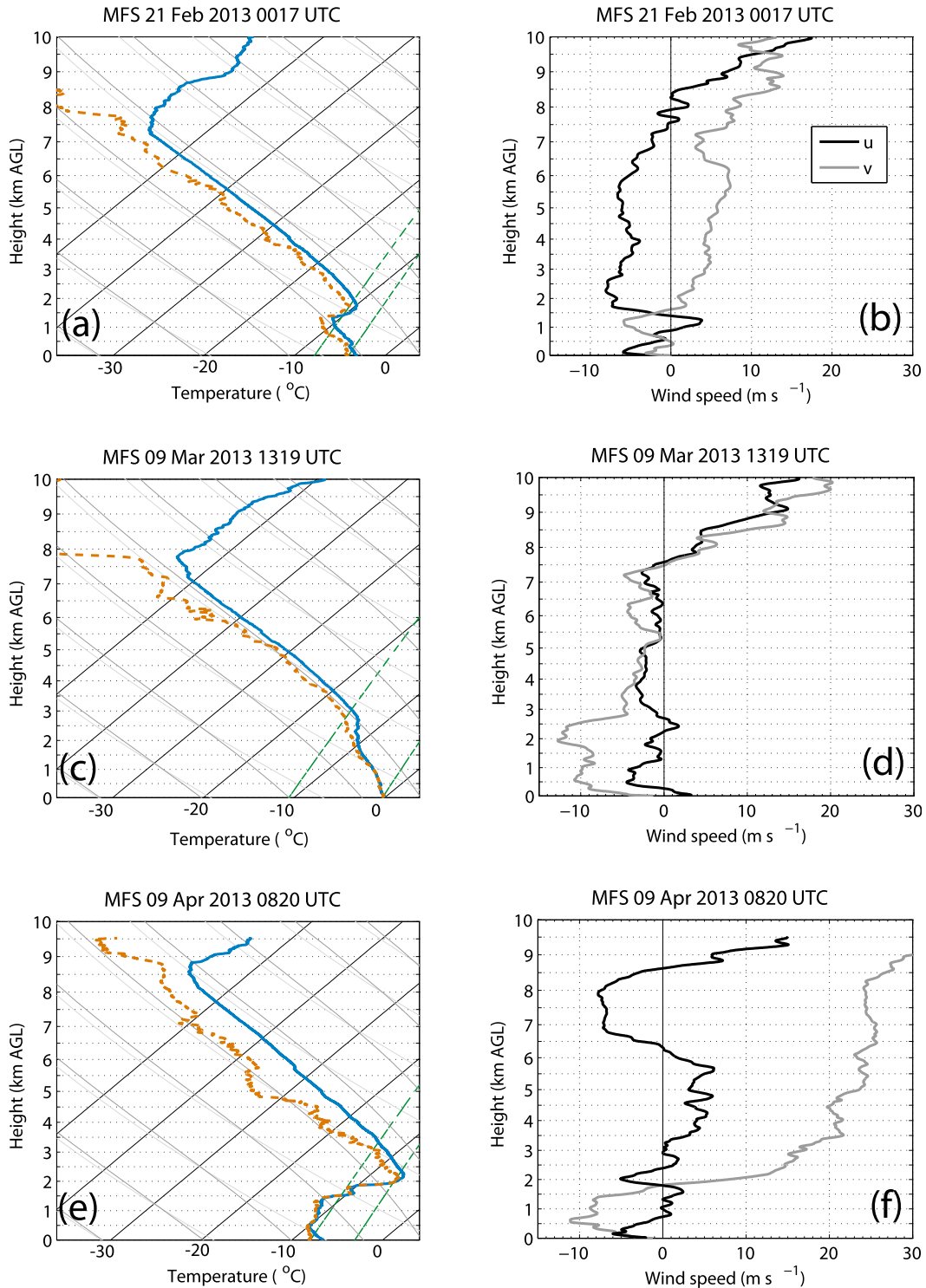


FIG. 7. Observed soundings from MFS at (a),(b) 0017 UTC 21 Feb 2013, (c),(d) 1319 UTC 9 Mar 2013, and (e),(f) 0820 UTC 9 Apr 2013, showing (left) skew- $T$  plots [with the vertical axis showing heights above the ground level, and with temperature (blue lines) and dewpoint temperature (orange lines) plotted along with selected mixing ratio lines, adiabats, and pseudo-adiabats] and (right) vertical profiles of the  $u$  (black lines) and  $v$  (gray lines) components of the wind.

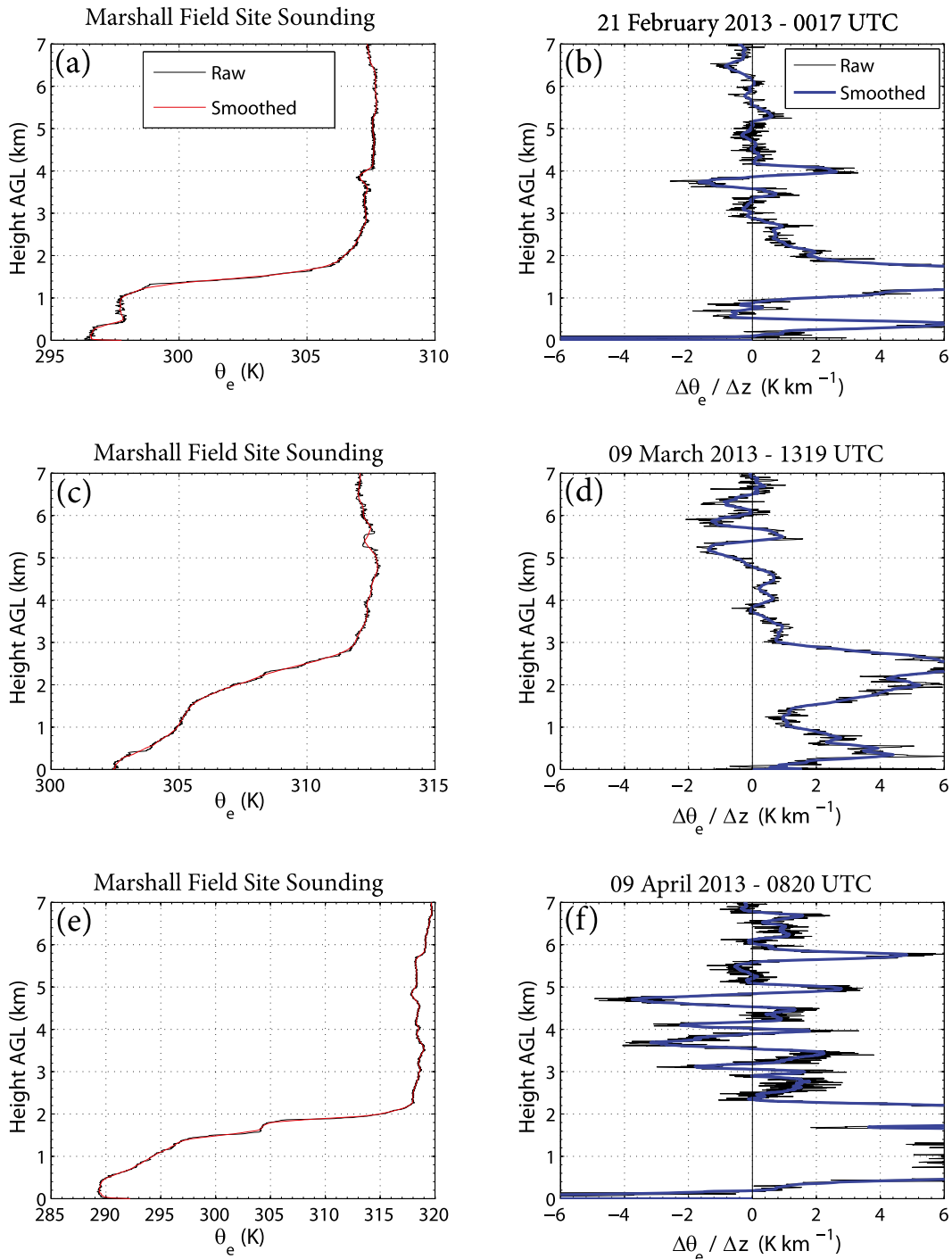


FIG. 8. (left) Raw (black lines) and smoothed (red lines) vertical profiles of  $\theta_e$  and (right) raw (black lines) and smoothed (blue lines) vertical profiles of the vertical gradient of  $\theta_e$  for the three soundings shown in Fig. 7: (a),(b) 0017 UTC 21 Feb 2013, (c),(d) 1319 UTC 9 Mar 2013, and (e),(f) 0820 UTC 9 Apr 2013. Note the extended abscissa scale in (e).

Another example of  $\theta_e$  and  $\partial\theta_e/\partial z$  profiles computed from the sounding launched at 0017 UTC 9 March 2013 is shown in Figs. 8c and 8d. Again, regions of potential instability are identified, this time in the layer

between approximately 5.0 and 6.5 km AGL (from  $-30.6^\circ$  to  $-44.9^\circ\text{C}$ ). The most negative values of  $\partial\theta_e/\partial z$  are approximately  $-2 \text{ K km}^{-1}$ . A CSU-CHILL vertical cross-sectional scan (RHI) taken in the direction of

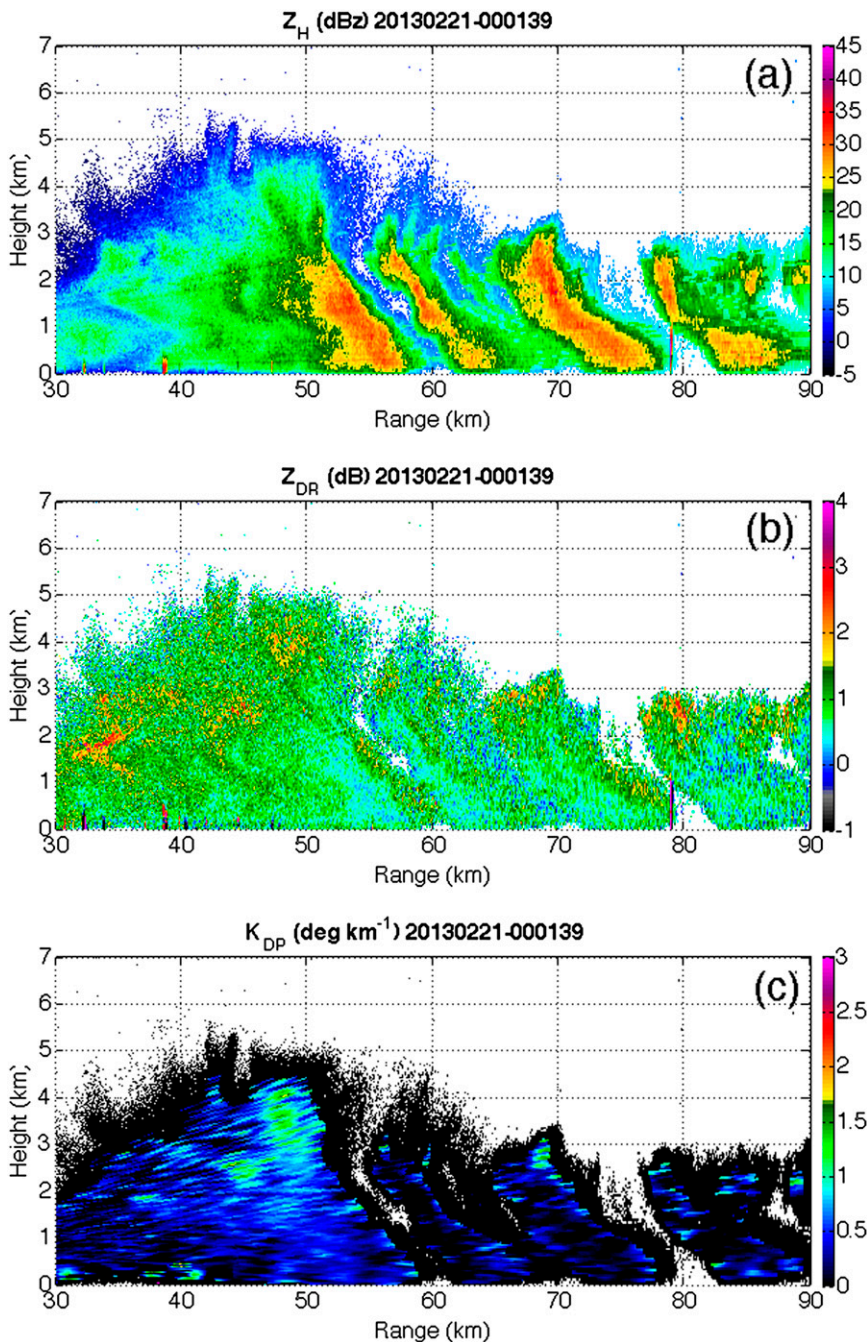


FIG. 9. CSU-CHILL RHI along the azimuth 181.7°, taken at 0001:39 UTC 21 Feb 2013: (a)  $Z_H$ , (b)  $Z_{DR}$ , and (c)  $K_{DP}$ .

MFS (Fig. 11) reveals generating cells that extend up to ~6.5 km AGL at the range of MFS (approximately 72 km), consistent with the diagnosed heights of potential instability from the sounding. Vertically pointing NCAR-XPOL data from about this time (Fig. 12) reveal positive vertical velocities from approximately 5 to 6 km, near the echo top, where  $Z_H$  values are

generally less than 5 dBZ. The mean vertical profile of Doppler velocity over the 3-min birdbath-scanning period shows positive vertical velocities above 5 km, indicating upward motion. Again, because of particle fall speeds, the actual vertical air motion likely is somewhat higher than  $1.0 \text{ m s}^{-1}$ . During these observations, the sounding crew made observations of “tiny graupel” and

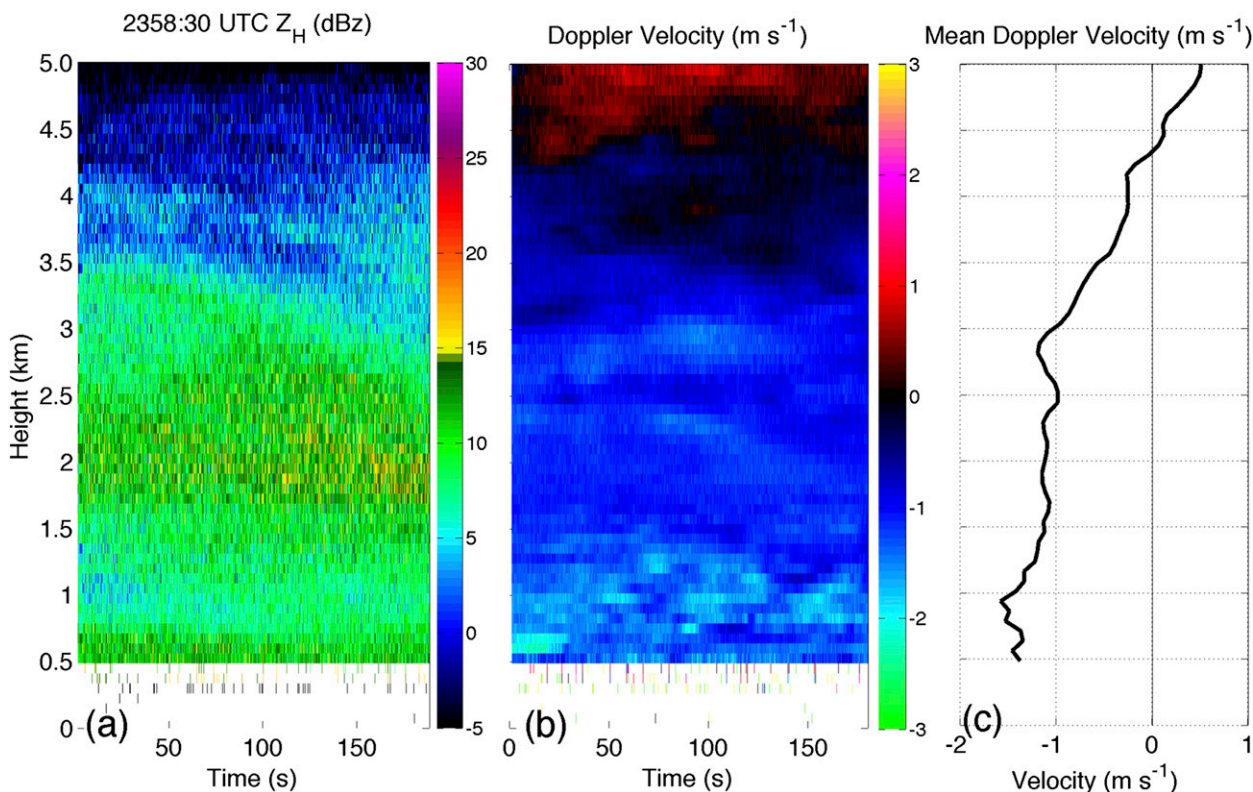


FIG. 10. Vertically pointing NCAR-XPOL data collected from 2355:22 to 2358:30 UTC 20 Feb 2013: (a)  $Z_H$ , (b) Doppler velocity, and (c) mean Doppler velocity over the 3-min scanning period, which corresponds to a translational distance of about 0.5–0.75 km for the generating cells as based on sounding-measured wind speeds.

heavily rimed dendritic or stellar snowflakes that retained some semblance of shape, along with small aggregates.

A final example of potential instability associated with observed generating cells comes from a snow storm that occurred on 9 April 2013. The vertical profile of  $\theta_e$  derived from an MFS sounding and the computed  $\partial\theta_e/\partial z$  profile at 0820 UTC are shown in Figs. 8e and 8f. The layer between approximately 3.0 and 5.0 km (from  $-11.1^\circ$  to  $-26.4^\circ\text{C}$ ) reveals negative  $\partial\theta_e/\partial z$ , with minimum values approaching  $-4\text{ K km}^{-1}$  at  $\sim 4.75\text{ km AGL}$  ( $-24.5^\circ\text{C}$ ). This corresponds well to the generating cells observed at this time with CSU-CHILL (Fig. 13) in the 4–6-km AGL layer. Unfortunately, vertically pointing radar data are not available for this case because of a power supply failure to the NCAR-XPOL. At the time of the sounding (and for at least 30 min afterward), very small ( $\sim 1\text{ mm}$  or less), high-density rimed particles were falling; the sounding crew could hear the sounds of the particles striking the sounding trailer. (Note that strong flow at low levels coupled with small terminal velocities of ice crystals means that substantial horizontal advection is possible.)

The FROST observations of generating cells occurring within or near layers of sounding-inferred potential

instability along with coincident vertically pointing radar data indicating upward motion in these same regions provide strong evidence to support the notion that generating cells are convective in nature, realizing potential instability often near echo top in winter storms. The observations presented herein of  $\sim 1\text{-km}$  horizontal and vertical dimensions of generating cells and estimated vertical velocities up to (and possibly exceeding)  $1\text{ m s}^{-1}$  within them are in excellent agreement with generating-cell characteristics that have been reported in the literature. The presence of rimed particles in at least three of the cases indicates that supercooled liquid water was present in some portion of the cloud. With the additional information provided by the polarimetric radar variables, we can explore the microphysical structure of generating cells. In the next section, we report on an interesting structure found in our dataset.

### c. Shroud echoes

In several of the FROST cases, the generating cells are enshrouded by a thin layer of enhanced  $Z_{DR}$  values that sometimes exceed 4 dB (Fig. 14). These enhancements in  $Z_{DR}$  appear on the periphery of the generating

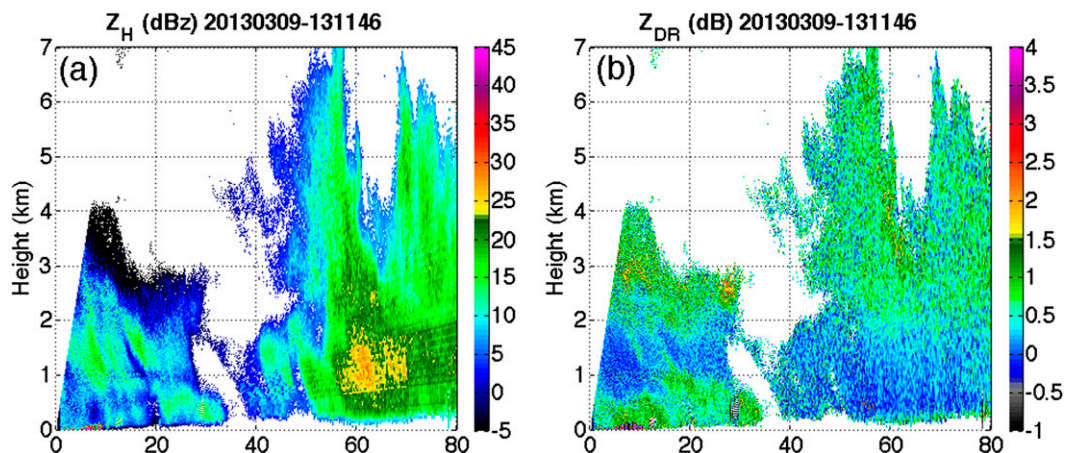


FIG. 11. CSU-CHILL RHI along the  $220.7^\circ$  azimuth at 1311 UTC 9 Mar 2013. The direction of the RHI is toward MFS (located at a range of approximately 72 km). Fields shown are (a)  $Z_H$  and (b)  $Z_{DR}$ .

cells (when viewed in vertical cross-sectional scans), collocated with smaller  $Z_H$  values. The largest measured  $Z_{DR}$  values are found for lower  $Z_H$  values; for example, data from Fig. 14 and the subsequent five RHI scans reveal that  $Z_{DR}$  does not exceed 3 dB for  $Z_H$  values in excess of about 12 dBZ. Note that such shroud echoes are not a result of Bragg scattering, which produces echoes characterized by  $Z_{DR} \sim 0$  dB because turbulent structures are isotropic on scales of 3 cm (i.e., that of the radar wavelength; Melnikov et al. 2011, 2013). Rather, they are presumably indicative of pristine anisotropic crystals at the periphery of the generating cells. Indeed, the  $Z_{DR}$  values exceeding  $\sim 4$ –5 dB are indicative of high-density, very anisotropic crystals such as plates or platelike dendrites (e.g., Hogan et al. 2002; Wolde and Vali 2001; Andrić et al. 2013).

In contrast to the high- $Z_{DR}$  periphery of shroud echoes, the cores tend to be characterized by higher  $Z_H$  and lower  $Z_{DR}$  values. Previous studies have identified the updraft cores of generating cells being collocated with the highest  $Z_H$  or SNR (e.g., Carbone and Bohne 1975; Cronce et al. 2007). Thus, if these updrafts are sufficiently strong to maintain the presence of supercooled liquid water, the liquid water content is expected to be largest within the updraft core in the center of the generating cell. As a result, the ice supersaturation would be maximized within the cores. According to the Bailey and Hallett (2009) ice crystal habit chart, there is no temperature at which higher supersaturations result in more isotropic particles (with intrinsic low  $Z_{DR}$ ) than do lower supersaturations. In other words, it is unlikely that a difference in vapor depositional growth conditions causes the  $Z_{DR}$  appearance of shroud echoes. The lower  $Z_{DR}$  in the cores of the generating-cell updrafts also are not a result of more chaotic tumbling of pristine crystals,

because spectrum-width values within the cores of generating cells remain low ( $< 1.0 \text{ m s}^{-1}$ ; see Fig. 15a), indicating a lack of significant turbulence within the cells. In fact, the largest spectrum-width values exist at  $\sim 2$  km AGL—a layer characterized by very large vertical wind shear (Fig. 15b). The possible role of vertical wind shear on the formation and structure of generating cells is discussed in the next section. Significant tumbling of crystals is also discounted because  $\rho_{hw}$  remains high within the generating cells (not shown), indicating a high degree of common alignment of particles and/or a lack of diversity of shapes within the radar sampling volume. If pristine anisotropic particles were tumbling,  $\rho_{hw}$  should be decreased. Mismatching between the H- and V-polarization beams is also unlikely, because beam patterns have been extensively studied for CSU-CHILL measurements at S band (e.g., Brangi et al. 2011). The X-band-only component used for this study is expected to have even better performance. Thus, beam mismatching is not a cause for concern, particularly with such weak  $Z_H$  gradients.

Therefore, at present, we favor riming and/or aggregation as a plausible explanation for the observed anticorrelation between  $Z_H$  and  $Z_{DR}$  in generating cells with shrouds. Recall from the introduction that supercooled liquid water and thus riming are possible given the sufficiently strong updrafts in generating cells. Also, the spatial correlation between updraft velocity and particle concentration found in previous studies implies that larger particles fall back through the updraft rather than being ejected from the top of the generating cell (e.g., Carbone and Bohne 1975), which is a favorable condition for collecting supercooled cloud droplets. Size sorting as larger rimed and/or aggregated particles fall out would lead to the smaller, more pristine (and thus

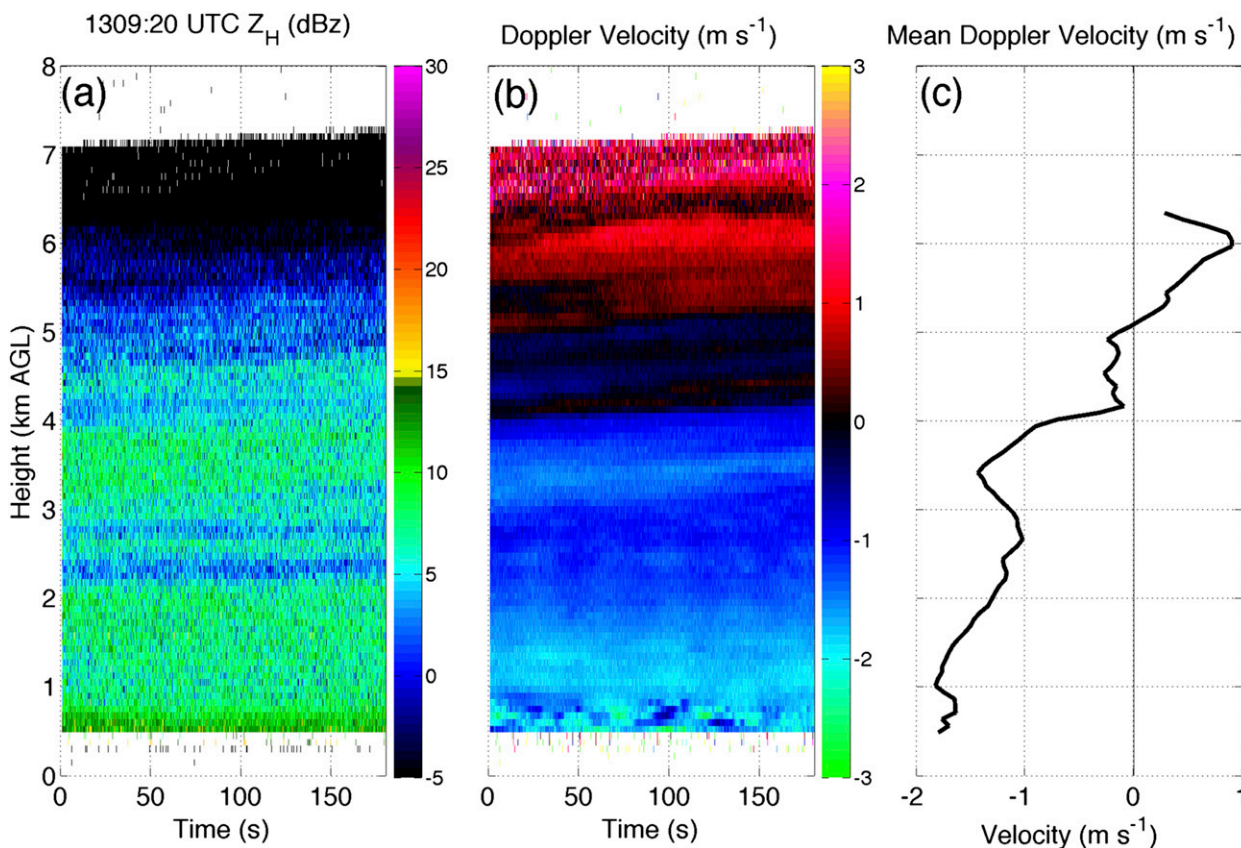


FIG. 12. Vertically pointing NCAR-XPOL data starting at 1306:12 UTC and ending at 1309:20 UTC 9 Mar 2013: (a)  $Z_H$ , (b) Doppler velocity, and (c) mean Doppler velocity over the 3-min birdbath-scanning period, which corresponds to a translational distance of about 1.3 km for the generating cells as based on sounding-measured wind speeds.

more anisotropic) crystals being left behind. The observations of rimed particles at MFS in each of the cases presented above demonstrate that riming of snow crystals was ongoing in the cloud. When ice crystals initiated in generating cells are of dendritic habit (which is expected around  $-15^{\circ}\text{C}$ ), rapid aggregation is also possible. There exists some ambiguity, because the polarimetric signatures of small rimed particles and aggregated snowflakes are very similar. Because both small graupel and aggregates were observed at the ground during FROST cases, we cannot say conclusively which microphysical process is dominant in each case. Thus, future studies employing in situ observations may be able to elucidate the particle types present in generating cells and allow for this important microphysical distinction.

These  $Z_{DR}$  shrouds around generating cells are not always observed. The habit of crystals grown in generating cells is dependent on the temperature and ice supersaturation attained. Thus, in some cases, the pristine crystals may not be sufficiently anisotropic to produce observable enhancements of  $Z_{DR}$ . In other cases, distance from the radar may preclude observations of enhanced

$Z_{DR}$  because of beam broadening (and thus signal domination by larger rimed particles and/or aggregates) or because of the shroud echo being below the minimum detectable reflectivity, which increases with increasing distance from the radar (e.g., Doviak and Zrníć 1993).

#### d. Evolution of generating cells

In addition to the standard scanning strategies employed during FROST, special series of RHI scans were collected using CSU-CHILL during a select few cases. These consecutive RHI scans were chosen to capture how the generating cells evolve rather than simply observing them at a “snapshot” in time (as in those cases above). One such implementation of consecutive RHI scans happened on 9 April 2013. Figure 16 shows the evolution of a particularly vigorous generating cell over a 10-min period starting at 2106:22 UTC. The radar operator admirably attempted to take RHI scans along the direction of the mean cell motion. Given the difficulty of this in practice, however, we caution that it is possible that the generating-cell motion had a component normal to the plane of the vertical cross section.

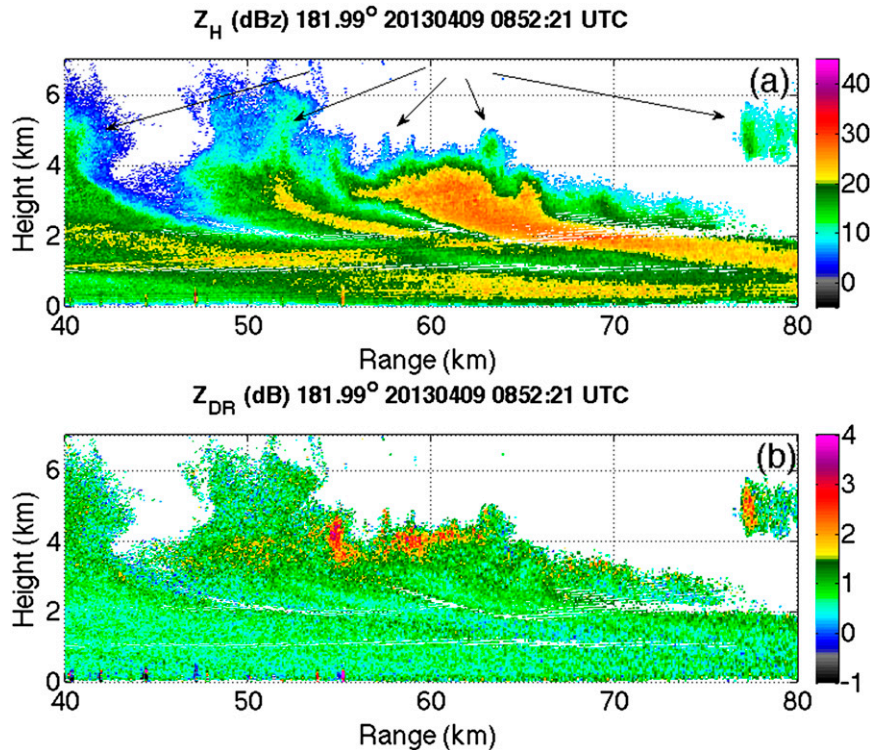


FIG. 13. CSU-CHILL RHI along the 181.99° azimuth at 0852 UTC 9 Apr 2013 for (a)  $Z_H$  and (b)  $Z_{DR}$ . Arrows show the locations of generating cells.

Nonetheless, if we assume that the generating cell remains perfectly within the cross-sectional plane over this 10-min period, we may compute the ascent rate of the echo top and attribute it solely to lofting of particles by the updraft. Figure 17 shows the measurable echo top as well as the heights of the 10- and 20-dBZ contours throughout this period. A simple calculation provides an estimate of the average ascent rate of  $2 \text{ m s}^{-1}$  over the first few scans, followed by leveling off, and finally descent. This estimate of updraft speed is consistent with previous observations from other FROST cases (described above) as well as those reported in the literature.

While the echo top remains quasi stationary from about 2109 through 2112 UTC the 10-dBZ contour continues to move upward (Fig. 17). This situation has the effect of sharpening the vertical gradient of  $Z_H$  over this time period. One possible interpretation of this tightening  $Z_H$  gradient is that particles within the generating cell are undergoing growth (perhaps through riming), whereas the updraft velocity of the cell is not increasing. This is also the time that a 20-dBZ contour appears in the cell, also signifying the growth of particles (and/or an increase in their concentration) in the lower portion of the cell. Between 2112:48 and 2114:24 UTC, the echo top remains nearly constant while the 10-dBZ

contour descends by  $\sim 200 \text{ m}$ , which in effect relaxes the  $Z_H$  gradient. This is consistent with fallout of the larger particles that have grown heavy enough to descend through the updraft (i.e., size sorting is ongoing, as suggested above for shroud echoes) in the absence of any significant change in updraft strength. After 2114:24 UTC, the generating cell diminishes in vertical extent, possibly as a result of updraft weakening and/or the cell moving out of the cross-sectional plane. The data presented in Figs. 16 and 17 suggest a lifetime on the order of at least 10 min for the generating cells.

The increase of  $Z_H$  toward the ground observed within this cell is consistent with the fingerprint of growth of particles through riming and/or aggregation. The  $Z_{DR}$  in this particular generating cell remained low throughout this period (not shown), implying the presence of rimed and/or aggregated particles. Because the top of the echo never displayed enhanced  $Z_{DR}$ , we favor the hypothesis that riming was ongoing. If aggregation was the dominant process in the generating cell, it must be occurring very rapidly, suggesting that dendrites would have to be the most likely pristine crystal type. The lack of a  $Z_{DR}$  or  $K_{DP}$  enhancement associated with the lower  $Z_H$  values at the periphery of the echoes (i.e., no shroud) indicates that

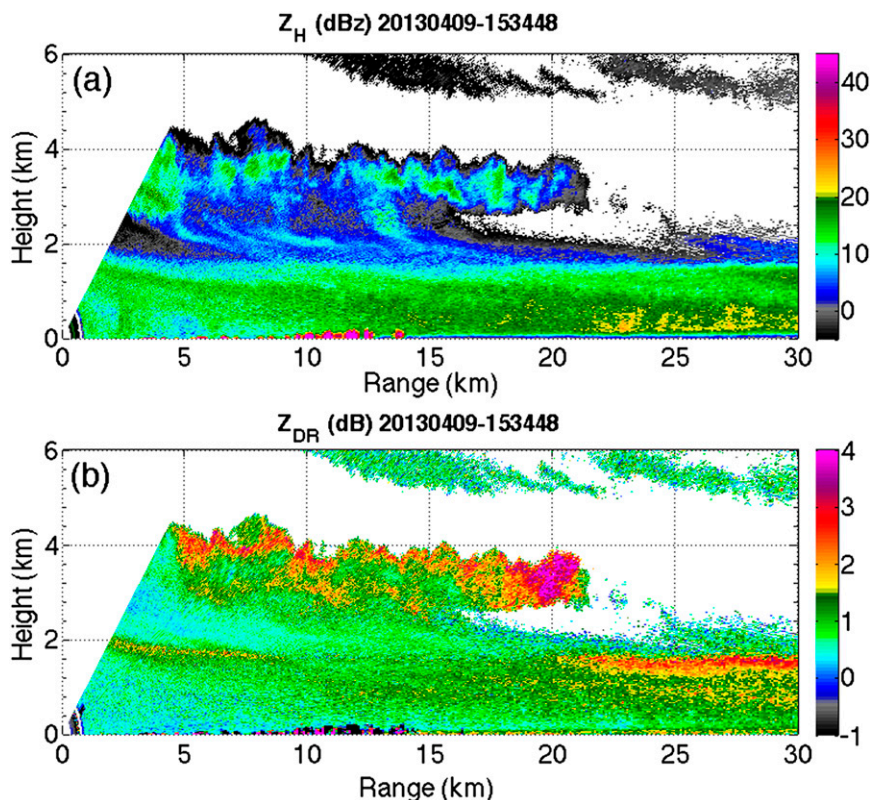


FIG. 14. CSU-CHILL RHI at 1534:48 UTC 9 Apr 2013, showing shroud echoes. Fields shown are (a)  $Z_H$  and (b)  $Z_{DR}$ .

dendrites were not present in significant concentrations. Indeed, the generating cell appeared at temperature levels inferred from the DNR sounding that are too cold for dendritic growth (i.e., colder than  $-22^{\circ}\text{C}$ ; Fig. 17). These temperatures are more consistent with the growth of crossed plates or assemblages of large plates and side planes (e.g., Bailey and Hallett 2009), which are more isometric “polycrystals” that tend to produce lower  $Z_{DR}$  and are less efficient at aggregation (e.g., Andrić et al. 2013).

#### 4. Discussion

There are at least two distinct modes of precipitation generation observed in the FROST cases. The first is shallow upslope flow, in which precipitation echoes are typically confined to a layer that is less than 2 km deep and is topped with a band of enhanced  $Z_{DR}$  (cf. Fig. 5). The vertical motion produced by upslope flow is typically only a few centimeters per second. The vertical structure of the polarimetric radar variables suggests initial depositional growth of dendritic crystals at the top of the layer, followed by rapid aggregation beneath (e.g., Kennedy and Rutledge 2011; Andrić et al. 2013). The

second mode is the generating cells that are the subject of this study. As seen above, updraft speeds in the generating cells are much larger than in the upslope flow cases, exceeding  $1\text{ m s}^{-1}$ . A natural question is, What proportion of the snow reaching the surface is produced by each of these two modes? In other words, How important is the role of ice nucleation in generating cells in comparison with shallower upslope flow layers? The stronger vertical velocities in generating cells are expected to be more efficient at activating ice nuclei; the available concentration of ice nuclei generally decreases with height in the troposphere, however, and generating cells tend to be located above the shallow upslope flow layer.

Previous studies have found that 20%–30% of the precipitation content reaching the ground is produced in generating cells, depending on their vertical velocity (Hobbs et al. 1980; Houze et al. 1981; Rutledge and Hobbs 1983). In our study, the limited radar data unfortunately prohibit reconstruction of the full three-dimensional structure of the storms. It is difficult to estimate the relative proportion of snow production from generating cells as compared with other parts of the storm from just a sample of RHI scans and PPI scans in each case. Although predominantly used for studying fast-evolving

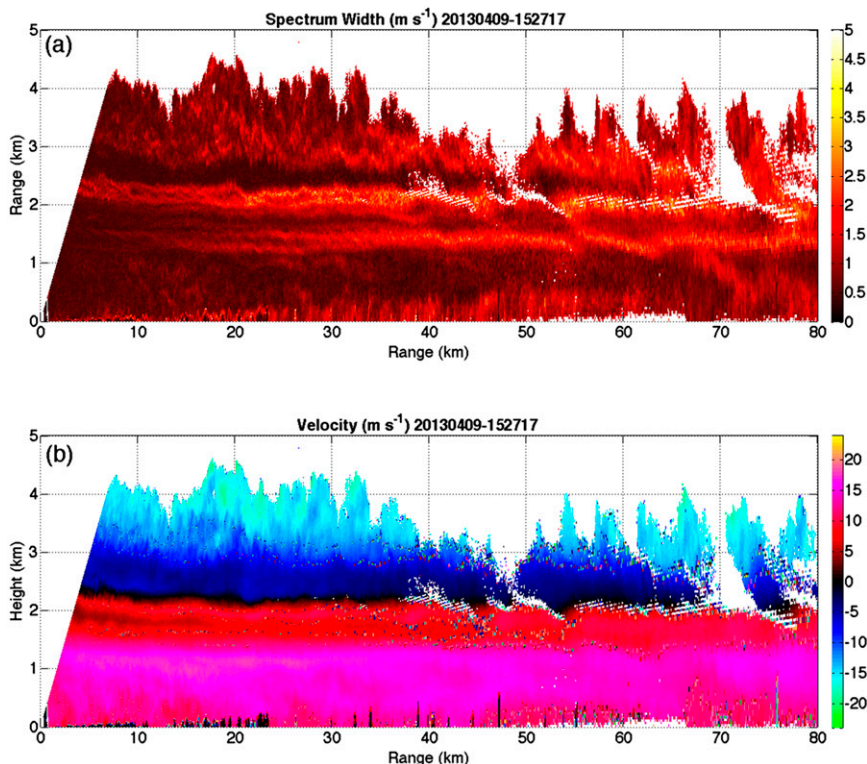


FIG. 15. As in Fig. 4, but for (a) Doppler spectrum width and (b) Doppler velocity.

severe convective storms and tropical cyclones, rapid-scanning polarimetric radars (e.g., Pazmany et al. 2013) could be used to provide high-resolution, volumetric scans of winter storms to investigate the precipitation efficiency and microphysical evolution of generating cells within such storms. Such research could have important implications for numerical weather prediction models, particularly winter quantitative precipitation estimation. If a nonnegligible portion of snowfall is generated by sub-1-km-scale structures, typical operational models employing comparatively coarse resolution may not be able to adequately resolve an important part of precipitation formation in winter storms. In addition, the riming and/or aggregation inferred from the radar measurements indicates that snow particles growing in generating cells will have larger fall speeds than crystals grown through vapor deposition, possibly contributing to a larger net precipitation flux to the surface. The possible presence of supercooled liquid water and the variety of particle types present within generating cells inferred from polarimetric radar measurements also should be understood in the context of their contributions to the radiative budget of winter storm clouds, particularly if not well simulated in traditional numerical models.

As we saw above, there was no preferred height or temperature level at which generating cells appeared in

each of the FROST cases. The only common characteristic about the location of their appearance is that they occurred near echo top. In the cases in which MFS soundings could corroborate the presence of potential instability, it was found to be in the same layers as the generating cells. Thus, one wonders *why* the potential instability exists in each case. The routine soundings from Denver (0000 and 1200 UTC) did not always show layers of potential instability. This may be because of the coarser resolution of these operational soundings, the representativeness of the environment, or other factors. The fact that the MFS soundings (launched into the snowing clouds) did show potential instability hints at the possibility that radiative effects at cloud top may be important for producing or maintaining generating cells. For example, we speculate that cloud-top cooling paired with heating associated with depositional and riming growth of snow crystals within the cloud could be a mechanism by which lapse rates are able to remain steep enough to maintain convection. In addition, advection of drier and/or cooler (i.e., lower  $\theta_e$ ) air aloft as a result of the synoptic pattern in most of these cases could play a role in producing the potential instability. Analysis of the evolution of the thermodynamic profiles from consecutive MFS soundings does indicate small decreases in  $\theta_e$  values over time in the layers containing potential instability and generating cells, although

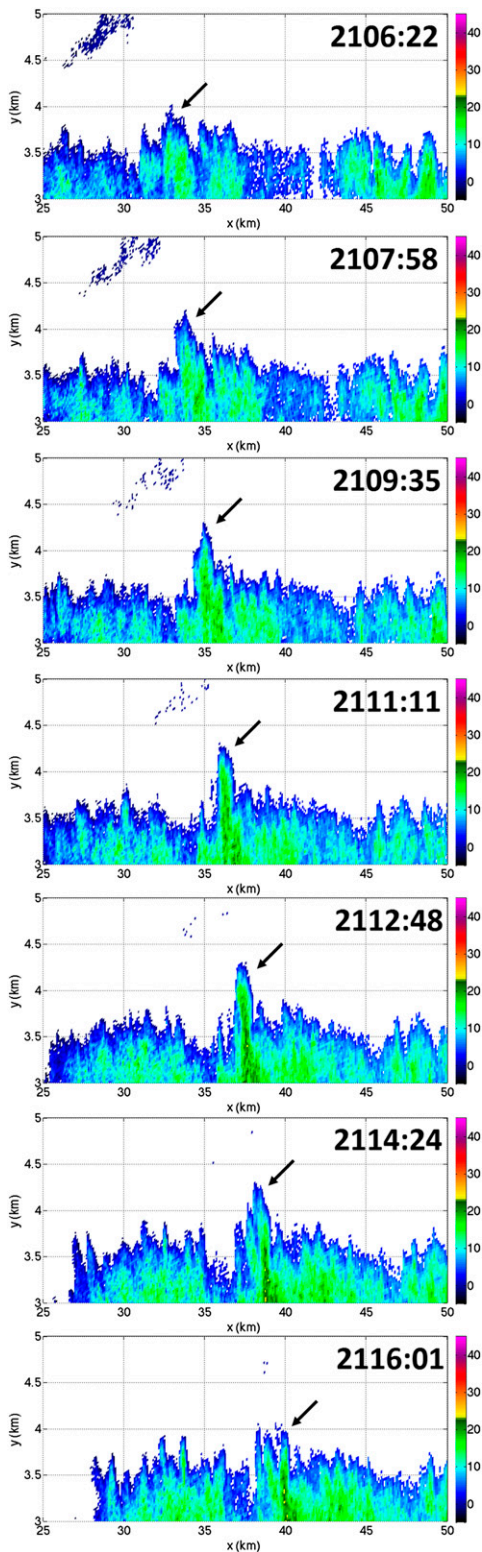


FIG. 16. Fields of  $Z_H$  from consecutive CSU-CHILL RHI scans over a 10-min period starting at 2106:22 UTC 9 Apr 2013 along the azimuth  $329.7^\circ$ . The arrow annotates the vigorous generating cell of interest.

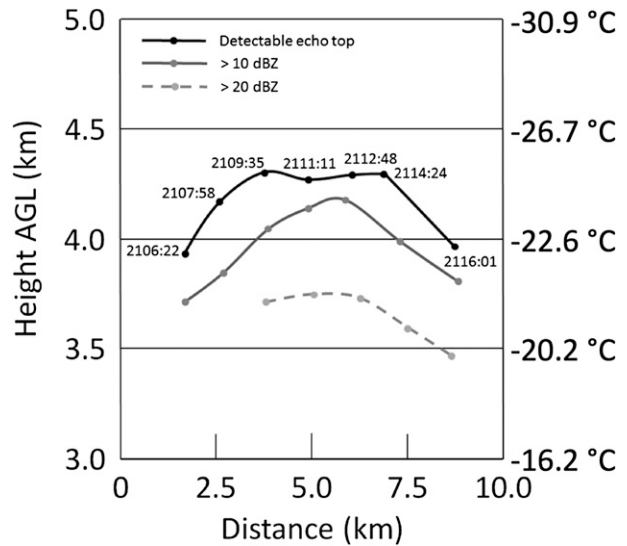


FIG. 17. Trace of the maximum vertical extent of selected contours of interest from the generating cell shown in Fig. 16. Scan times are annotated next to the markers. Contours shown are for the measurable echo top (black solid curve), the 10-dBZ contour (dark-gray solid curve), and the 20-dBZ contour (gray dashed curve). Corresponding temperatures from each height are taken from the 0000 UTC 10 Apr 2013 operational DNR sounding.

the observations are inconclusive as to whether this is because of advection or other effects. Potential instability is not found at the top of the shallow upslope layer because often there is a sharp inversion overlying this layer; thus, it is too stable for radiative effects to generate or maintain potential instability. In contrast, the environmental lapse rate above the upslope layer was always near moist adiabatic (because of radiative–convective equilibrium); therefore, it would not take much heating/cooling or advection of low- $\theta_e$  air to generate convective instability near cloud top. Future modeling studies should pay attention to radiative effects and the large-scale forcing to explore their possible roles in generating and/or maintaining potential instability at cloud top.

Another factor to consider is the possible role of vertical wind shear. In most of the cases, a large amount of vertical wind shear existed near the layer with the inversion (cf. Figs. 7 and 15) where winds change from predominantly northerly at low levels to southerly aloft. Houze and Medina (2005) found cellular updrafts above the melting layer in their study of winter midlatitude frontal systems in the Pacific Northwest. They suggest that shear-induced turbulence may serve as a source for the rising motion. In addition, the authors suggest that a layer of turbulence may also affect the hydrometeors passing through by increased aggregation and possible riming.

The appearance of the generating cells themselves suggests that they are not strongly influenced by vertical

wind shear, as the cells are upright in every case (i.e., there is no evidence for tilting). Also, the soundings in Fig. 7 demonstrate that wind shear is considerably smaller in the layers in which generating cells occurred, at least in those three cases. Thus, it appears unlikely that vertical wind shear plays a role in the structure or appearance of the generating cells. Note that the vertically pointing Doppler radar data revealed updrafts near cloud top, up to several kilometers above the shear layer. The shear layers themselves did not exhibit substantial upward vertical motion. We cannot, however, rule out the possibility that some mechanism similar to that proposed by Houze and Medina (2005) may be acting on the hydrometeors formed aloft that subsequently descend through the shear layer.

Recent observations from the Profiling of Winter Storms (PLOWs) experiment using the high-resolution, vertically pointing, airborne “Wyoming Cloud Radar” system have shown a frequent occurrence of generating cells in midlatitude cyclones (e.g., Plummer et al. 2013; Rosenow et al. 2014). Generating-cell characteristics found in those cases are in very good agreement with those found in our Colorado storm cases analyzed here. This result suggests that generating cells have characteristic scales (width, height, and updraft speed) that do not vary much, even in different geographical areas. In addition, it demonstrates that generating cells indeed are very common in all types of snowstorms, in various parts of the United States. Future studies employing high-resolution radar in other regions may confirm the common presence of generating cells in snowstorms.

The frequent occurrence of updraft turrets near echo tops found in this study is important for aviation concerns. In addition to the possible turbulence generated by convective motions at echo top, generating cells may provide a possible sustained source of supercooled liquid water that may pose an icing hazard to aircraft. Indeed, the radar data suggest ongoing riming in some of the generating cells, providing strong evidence that supercooled liquid water was present in at least some of the FROST cases. Aircraft or other in situ observations can help to clarify the particle types and amount of supercooled liquid water present in generating cells. If supercooled liquid water is a common occurrence within generating cells, soundings may be used to identify layers of potential instability where generating cells are likely to grow so as to forecast potential icing hazards.

## 5. Summary

Coordinated observations in 19 winter-storm cases were obtained during the 2013 Front Range Orographic

Storms project. Measurements included special soundings and radar observations from two research X-band polarimetric radars: NCAR-XPOL and CSU-CHILL. We present some of the high-resolution polarimetric radar data of snow-generating cells collected during FROST. The main conclusions of this study may be summarized as follow:

- 1) Generating cells were found in every FROST case (19 total), indicating that they are very common (if not ubiquitous) in snowstorms. In a typical case, these generating cells were located in deeper clouds, often overlying a shallow layer of upslope flow.
- 2) Characteristics of generating cells include  $\sim 1$ -km horizontal and vertical dimensions and updraft speeds on the order of  $1\text{--}2\text{ m s}^{-1}$ . These scales are in good accord with previous studies. In addition, “rapid scan” observations revealed lifetimes of individual convective turrets that are on the order of at least  $\sim 10$  min.
- 3) When corroborating soundings were available, the locations of generating cells were found within cloud-top layers containing potential instability. We speculate that radiative effects are important for the maintenance of such instability (and thus generating cells).
- 4) At present, our observations suggest that vertical wind shear may play only a limited role in the appearance or structure of generating cells. High-resolution numerical simulations may be used to further explore the role of vertical shear.
- 5) In some cases, the generating cells were enshrouded by a thin layer of enhanced  $Z_{DR}$  indicative of pristine, anisotropic ice crystals such as plates or dendrites. The anticorrelation between  $Z_H$  and  $Z_{DR}$  in these shroud echoes is suggestive of ongoing riming and/or aggregation within the core of the generating cells. Rimed particles were observed at the ground in at least three of these cases. Figure 18 is a conceptual model of a generating cell with a shroud echo.
- 6) The implied presence of supercooled liquid water within generating cells and their frequency of occurrence have important implications for numerical modeling efforts and for aviation icing concerns.

*Acknowledgments.* The authors thank Francesc Junyent, Jim George, and Dave Brunkow (CSU) for their help with the CSU-CHILL data processing and transfer, as well as Nancy Rehak (NCAR) for assistance in operating the NCAR-XPOL radar. We are grateful to Chris Davis (NCAR) and the Advanced Study Program for funding that supported the radiosondes and to Paul Ciesielski (CSU) for lending us the CSU radiosonde system. Additional funding for this project comes from

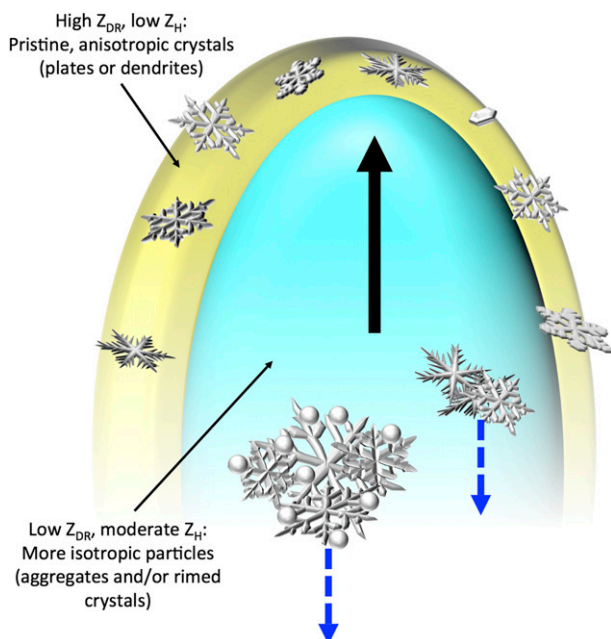


FIG. 18. Conceptual model of a vertical slice through a generating cell with a shroud echo with example particle types present. The shroud of large  $Z_{DR}$  and low  $Z_H$  values (yellow color) indicates the presence of pristine, anisotropic crystals with platelike or dendritic habits. The core of the generating cell (bluish color) is characterized by low  $Z_{DR}$  and moderate  $Z_H$ , indicating more isotropic particles such as snow aggregates or rimed crystals, the largest of which are descending (blue dashed lines). The core is also where the strongest updraft speeds (and thus supersaturations with respect to ice) are located, indicated by the black vertical arrow. See also the “particle fountain” schematic of Yuter and Houze (1995).

NSF Grant AGS-1143948 (MK) and the CSU-CHILL Cooperative Agreement AGS-1138116 (SR and PK). Students from Metropolitan State University of Denver, including Bryce Verreyen, Mary Lambert, and Alycia Gilliland, are thanked for their help with the sounding launches, as are Dan Stern, Mike Kavulich, and Scott Landolt (NCAR). Technical assistance from Kara Sulia (Princeton) and Zach Lebo (NOAA/CIRES) is appreciated. We also thank the three anonymous reviewers for their constructive and helpful comments that improved the quality and clarity of the manuscript. This paper is dedicated to the memory of Robert H. Jump.

## APPENDIX

### NCAR-XPOL Radar

The NCAR X-band Polarimetric (NCAR-XPOL) radar is a transportable polarimetric Doppler radar manufactured by ProSensing, Inc. It was placed at the Marshall Field Site for the duration of the FROST experiment and was controlled remotely. Selected technical specifications

TABLE A1. Selected technical specifications and operating configurations for the NCAR-XPOL radar.

Frequency	9.41 GHz (X band)
Wavelength	3.2 cm
Antenna diameter	1.8 m
3-dB beamwidth	1.35°
Transmitter type	Magnetron
Peak power	20 kW
Duty cycle	0.1%
Polarization	Simultaneous H and V
Pulse repetition time	0.5 ms
Pulse width	1.0 $\mu$ s
Range spacing	75 m
Azimuthal sampling resolution (PPIs)	0.8°
Elevation sampling resolution (RHIs)	0.2°
No. of samples per ray	64
Max unambiguous range	75.0 km
Nyquist velocity	15.9 $\text{m s}^{-1}$

of the NCAR-XPOL, as well as some of the operating characteristics employed during FROST, are provided in Table A1.

## REFERENCES

- Andrić, J., M. R. Kumjian, D. S. Zrnić, J. M. Straka, and V. M. Melnikov, 2013: Polarimetric signatures above the melting layer in winter storms: An observational and modeling study. *J. Appl. Meteor. Climatol.*, **52**, 682–700, doi:10.1175/JAMC-D-12-028.1.
- Bailey, M. P., and J. Hallett, 2009: A comprehensive habit diagram for atmospheric ice crystals: Confirmation from the laboratory, AIRS II, and other field studies. *J. Atmos. Sci.*, **66**, 2888–2899, doi:10.1175/2009JAS2883.1.
- Bechini, R., L. Baldini, and V. Chandrasekar, 2013: Polarimetric radar observations in the ice region of precipitating clouds at C-band and X-band radar frequencies. *J. Appl. Meteor. Climatol.*, **52**, 1147–1169, doi:10.1175/JAMC-D-12-055.1.
- Bringi, V. N., and V. Chandrasekar, 2001: *Polarimetric Doppler Weather Radar*. 1st ed. Cambridge University Press, 636 pp.
- , R. Hoferer, D. A. Brunkow, R. Schwerdtfeger, V. Chandrasekar, S. A. Rutledge, and J. George, 2011: Design and performance characteristics of the new 8.5-m dual-offset Gregorian antenna for the CSU-CHILL radar. *J. Atmos. Oceanic Technol.*, **28**, 907–920, doi:10.1175/2011JTECHA1493.1.
- Browning, K. A., and T. W. Harrold, 1969: Air motion and precipitation growth in a wave depression. *Quart. J. Roy. Meteor. Soc.*, **95**, 288–309, doi:10.1002/qj.49709540405.
- Carbone, R. E., and A. R. Bohne, 1975: Cellular snow generation—A Doppler radar study. *J. Atmos. Sci.*, **32**, 1384–1394, doi:10.1175/1520-0469(1975)032<1384:CSGDRS>2.0.CO;2.
- Cronce, M., R. M. Rauber, K. R. Knupp, B. F. Jewett, J. T. Walters, and D. Phillips, 2007: Vertical motions in precipitation bands in three winter cyclones. *J. Appl. Meteor. Climatol.*, **46**, 1523–1543, doi:10.1175/JAM2533.1.
- Crosier, J., and Coauthors, 2013: Microphysical properties of cold frontal rainbands. *Quart. J. Roy. Meteor. Soc.*, doi:10.1002/qj.2206, in press.
- Douglas, R. H., K. L. S. Gunn, and J. S. Marshall, 1957: Pattern in the vertical of snow generation. *J. Meteor.*, **14**, 95–114, doi:10.1175/1520-0469(1957)014<0095:PITVOS>2.0.CO;2.

- Doviak, R. J., and D. S. Zrnić, 1993: *Doppler Radar and Weather Observations*. 2nd ed. Academic Press, 562 pp.
- Evans, A. G., J. D. Locatelli, M. T. Stoelinga, and P. V. Hobbs, 2005: The IMPROVE-1 storm of 1–2 February 2001. Part II: Cloud structures and the growth of precipitation. *J. Atmos. Sci.*, **62**, 3456–3473, doi:10.1175/JAS3547.1.
- Gunn, K. L. S., M. P. Langleben, A. S. Dennis, and B. A. Power, 1954: Radar evidence of a generating level for snow. *J. Meteor.*, **11**, 20–26, doi:10.1175/1520-0469(1954)011<0020:REOAGL>2.0.CO;2.
- Henriou, X., H. Sauvageot, and D. Ramond, 1978: Fine-structure of precipitation and temperature in a stratocumulus cloud. *J. Atmos. Sci.*, **35**, 2315–2324, doi:10.1175/1520-0469(1978)035<2315:FOPATI>2.0.CO;2.
- Herzogh, P. H., and P. V. Hobbs, 1981: The mesoscale and microscale structure and organization of clouds and precipitation in midlatitude cyclones. IV: Vertical air motions and microphysical structures of prefrontal surge clouds and cold-frontal clouds. *J. Atmos. Sci.*, **38**, 1771–1784, doi:10.1175/1520-0469(1981)038<1771:TMAMSA>2.0.CO;2.
- Heymfield, A. J., and R. G. Knollenberg, 1972: Properties of cirrus generating cells. *J. Atmos. Sci.*, **29**, 1358–1366, doi:10.1175/1520-0469(1972)029<1358:POCGC>2.0.CO;2.
- Hobbs, P. V., and J. D. Locatelli, 1978: Rainbands, precipitation cores, and generating cells in a cyclonic storm. *J. Atmos. Sci.*, **35**, 230–241.
- , T. J. Matejka, P. H. Herzogh, J. D. Locatelli, and R. A. Houze Jr., 1980: The mesoscale and microscale structure and organization of clouds and precipitation in midlatitude cyclones. I: A case study of a cold front. *J. Atmos. Sci.*, **37**, 568–596, doi:10.1175/1520-0469(1980)037<0568:TMAMSA>2.0.CO;2.
- Hogan, R., P. Field, A. Illingworth, R. Cotton, and T. Choullarton, 2002: Properties of embedded convection in warm-frontal mixed-phase cloud from aircraft and polarimetric radar. *Quart. J. Roy. Meteor. Soc.*, **128**, 451–476, doi:10.1256/003590002321042054.
- Houze, R. A., Jr., and S. Medina, 2005: Turbulence as a mechanism for orographic precipitation enhancement. *J. Atmos. Sci.*, **62**, 3599–3623, doi:10.1175/JAS3555.1.
- , J. D. Locatelli, and P. V. Hobbs, 1976: Dynamics and cloud microphysics of the rainbands in an occluded frontal system. *J. Atmos. Sci.*, **33**, 1921–1936, doi:10.1175/1520-0469(1976)033<1921:DACMOT>2.0.CO;2.
- , S. A. Rutledge, T. J. Matejka, and P. V. Hobbs, 1981: The mesoscale and microscale structure and organization of clouds and precipitation in midlatitude cyclones. III: Air motions and precipitation growth in a warm-frontal rainband. *J. Atmos. Sci.*, **38**, 639–649, doi:10.1175/1520-0469(1981)038<0639:TMAMSA>2.0.CO;2.
- Ikeda, K., R. M. Rasmussen, W. D. Hall, and G. Thompson, 2007: Observations of freezing drizzle in extratropical cyclonic storms during IMPROVE-2. *J. Atmos. Sci.*, **64**, 3016–3043, doi:10.1175/JAS3999.1.
- Junyent, F., V. Chandrasekar, P. Kennedy, S. Rutledge, V. Bringi, J. George, and D. Brunkow, 2013: Salient features of the CSU-CHILL radar X-band channel upgrade. *Proc. 36th Conf. on Radar Meteorology*, Breckenridge, CO, Amer. Meteor. Soc., 2B.6. [Available online at <https://ams.confex.com/ams/36Radar/webprogram/Paper229162.html>.]
- Kennedy, P. C., and S. A. Rutledge, 2011: S-band dual-polarization radar observations of winter storms. *J. Appl. Meteor. Climatol.*, **50**, 844–858, doi:10.1175/2010JAMC2558.1.
- Kumjian, M. R., 2013a: Principles and applications of dual-polarization weather radar. Part I: Description of the polarimetric radar variables. *J. Oper. Meteor.*, **1**, 226–242, doi:10.15191/nwajom.2013.0119.
- , 2013b: Principles and applications of dual-polarization weather radar. Part II: Warm and cold season applications. *J. Oper. Meteor.*, **1**, 243–264, doi:10.15191/nwajom.2013.0120.
- , 2013c: Principles and applications of dual-polarization weather radar. Part III: Artifacts. *J. Oper. Meteor.*, **1**, 265–274, doi:10.15191/nwajom.2013.0121.
- Lamb, D., and J. Verlinde, 2011: *Physics and Chemistry of Clouds*. 1st ed. Cambridge University Press, 584 pp.
- Langleben, M. P., 1956: The plan pattern of snow echoes at the generating level. *J. Meteor.*, **13**, 554–560, doi:10.1175/1520-0469(1956)013<0554:TPPOSE>2.0.CO;2.
- Ludlam, F. H., 1956: The form of ice clouds: II. *Quart. J. Roy. Meteor. Soc.*, **82**, 257–265, doi:10.1002/qj.49708235302.
- Marshall, J. S., 1953: Precipitation trajectories and patterns. *J. Atmos. Sci.*, **10**, 25–29, doi:10.1175/1520-0469(1953)010<0025:PTAP>2.0.CO;2.
- Matejka, T. J., R. A. Houze Jr., and P. V. Hobbs, 1980: Microphysics and dynamics of clouds associated with mesoscale rainbands in extratropical cyclones. *Quart. J. Roy. Meteor. Soc.*, **106**, 29–56, doi:10.1002/qj.49710644704.
- Melnikov, V. M., R. J. Doviak, D. S. Zrnić, and D. J. Stensrud, 2011: Mapping Bragg scatter with a polarimetric WSR-88D. *J. Atmos. Oceanic Technol.*, **28**, 1273–1285, doi:10.1175/JTECH-D-10-05048.1.
- , —, —, and —, 2013: Structures of Bragg scatter observed with the polarimetric WSR-88D. *J. Atmos. Oceanic Technol.*, **30**, 1253–1258, doi:10.1175/JTECH-D-12-00210.1.
- Miles, V. G., 1956: Interpretation of the height-versus-time presentation of radar echoes. *J. Meteor.*, **13**, 362–368, doi:10.1175/1520-0469(1956)013<0362:IOTHVT>2.0.CO;2.
- Pazmany, A. L., J. B. Mead, H. B. Bluestein, J. C. Snyder, and J. B. Houser, 2013: A mobile rapid-scanning X-band polarimetric (RaXPol) Doppler radar system. *J. Atmos. Oceanic Technol.*, **30**, 1398–1413, doi:10.1175/JTECH-D-12-00166.1.
- Plummer, D. M., R. M. Rauber, G. M. McFarquhar, B. F. Jewett, and D. Leon, 2013: The structure and role of generating cells and precipitation bands in cold-season midlatitude cyclones. *Proc. 25th Conf. on Mesoscale Meteorology*, Portland, OR, Amer. Meteor. Soc., 11.3. [Available online at <https://ams.confex.com/ams/15MESO/webprogram/Paper227744.html>.]
- Rasmussen, R. M., B. C. Bernstein, M. Murakami, G. Stossmeister, and J. Reisner, 1995: The 1990 Valentine’s Day Arctic outbreak. Part I: Mesoscale and microscale structure and evolution of a Colorado Front Range shallow upslope cloud. *J. Appl. Meteor.*, **34**, 1481–1511, doi:10.1175/1520-0450-34.7.1481.
- , and Coauthors, 2012: How well are we measuring snow: The NOAA/FAA/NCAR winter precipitation test bed. *Bull. Amer. Meteor. Soc.*, **93**, 811–829, doi:10.1175/BAMS-D-11-00052.1.
- Rosenow, A. A., D. M. Plummer, R. M. Rauber, G. M. McFarquhar, B. F. Jewett, and D. C. Leon, 2014: Vertical velocity and physical structure of generating cells and convection in the comma head region of continental winter cyclones. *J. Atmos. Sci.*, doi:10.1175/JAS-D-13-0249.1, in press.
- Rutledge, S. A., and P. V. Hobbs, 1983: The mesoscale and microscale structure and organization of clouds and precipitation in midlatitude cyclones. VIII: A model for the “seeder-feeder” process in warm-frontal rainbands. *J. Atmos. Sci.*, **40**, 1185–1206, doi:10.1175/1520-0469(1983)040<1185:TMAMSA>2.0.CO;2.

- Ryzhkov, A. V., T. J. Schuur, D. W. Burgess, P. L. Heinselman, S. E. Giangrande, and D. S. Zrnić, 2005: The Joint Polarization Experiment: Polarimetric rainfall measurements and hydrometeor classification. *Bull. Amer. Meteor. Soc.*, **86**, 809–824, doi:10.1175/BAMS-86-6-809.
- Sassen, K. C., J. Grund, J. D. Spinhirne, M. M. Hardesty, and J. M. Alvarez, 1990: The 27–28 October 1986 FIRE IFO cirrus case study: A five lidar overview of cloud structure and evolution. *Mon. Wea. Rev.*, **118**, 2288–2311, doi:10.1175/1520-0493(1990)118<2288:TOFICC>2.0.CO;2.
- Schneebeil, M., N. Dawes, M. Lehning, and A. Berne, 2013: High-resolution vertical profiles of X-band polarimetric radar observables during snowfall in the Swiss Alps. *J. Appl. Meteor. Climatol.*, **52**, 378–394, doi:10.1175/JAMC-D-12-015.1.
- Stark, D., B. A. Colle, and S. E. Yuter, 2013: Observed microphysical evolution for two East Coast winter storms and the associated snow bands. *Mon. Wea. Rev.*, **141**, 2037–2057, doi:10.1175/MWR-D-12-00276.1.
- Straka, J. M., D. S. Zrnić, and A. V. Ryzhkov, 2000: Bulk hydrometeor classification and quantification using polarimetric radar data: Synthesis of relations. *J. Appl. Meteor.*, **39**, 1341–1372, doi:10.1175/1520-0450(2000)039<1341:BHCAQU>2.0.CO;2.
- Syrett, W. J., B. A. Albrecht, and E. E. Clothiaux, 1995: Vertical cloud structure in a midlatitude cyclone from a 94-GHz radar. *Mon. Wea. Rev.*, **123**, 3393–3407, doi:10.1175/1520-0493(1995)123<3393:VCSIAM>2.0.CO;2.
- Wang, Y., and V. Chandrasekar, 2009: Algorithm for estimation of the specific differential phase. *J. Atmos. Oceanic Technol.*, **26**, 2565–2578, doi:10.1175/2009JTECHA1358.1.
- Wexler, R., and D. Atlas, 1959: Precipitation generating cells. *J. Atmos. Sci.*, **16**, 327–332, doi:10.1175/1520-0469(1959)016<0327:PGC>2.0.CO;2.
- Wolde, M., and G. Vali, 2001: Polarimetric signatures from ice crystals observed at 95 GHz in winter clouds. Part II: Frequencies of occurrence. *J. Atmos. Sci.*, **58**, 842–849, doi:10.1175/1520-0469(2001)058<0842:PSFICO>2.0.CO;2.
- Yuter, S. E., and R. A. Houze Jr., 1995: Three-dimensional kinematic and microphysical evolution of Florida cumulonimbus. Part III: Vertical mass transport, mass divergence, and synthesis. *Mon. Wea. Rev.*, **123**, 1964–1983, doi:10.1175/1520-0493(1995)123<1964:TDKAME>2.0.CO;2.
- Zrnić, D. S., and A. V. Ryzhkov, 1999: Polarimetry for weather surveillance radars. *Bull. Amer. Meteor. Soc.*, **80**, 389–406, doi:10.1175/1520-0477(1999)080<0389:PFWSR>2.0.CO;2.